Constraints on galactic wind models

Constraints on galactic wind models

Avery Meiksin

SUPA★, Institute for Astronomy, University of Edinburgh, Blackford Hill, Edinburgh EH9 3HJ, UK

17 June 2016

ABSTRACT

Observational implications are derived for two standard models of supernovae-driven galactic winds: a freely expanding steady-state wind and a wind sourced by a self-similarly expanding superbubble including thermal heat conduction. It is shown that, for the steady-state wind, matching the measured correlation between the soft x-ray luminosity and star formation rate of starburst galaxies is equivalent to producing a scaled wind mass-loading factor relative to the star-formation rate of 0.5–3, in agreement with the amount inferred from metal absorption line measurements. The match requires the asymptotic wind velocity v_∞ to scale with the star formation rate $\dot{M}_*$ (in $M_\odot \, \mathrm{yr}^{-1}$) approximately as $v_\infty \simeq (700 - 1000) \, \mathrm{km \, s^{-1}} \, \dot{M}_*^{1/6}$. The implied mass injection rate is close to the amount naturally provided by thermal evaporation from the wall of a superbubble in a galactic disc, suggesting thermal evaporation may be a major source of mass-loading. The predicted mass-loading factors from thermal evaporation within the galactic disc alone, however, are somewhat smaller, 0.2–2, so that a further contribution from cloud ablation or evaporation within the wind may be required. Both models may account for the 1.4 GHz luminosity of unresolved radio sources within starburst galaxies for plausible parameters describing the distribution of relativistic electrons. Further observational tests to distinguish the models are suggested.

Key words: galaxies: starburst – galaxies: star formation – X-rays: galaxies – X-rays: ISM – radio continuum: galaxies – radio continuum: ISM

1 INTRODUCTION

Galactic winds have been known to be common features of star-forming galaxies for many years. While particularly spectacular winds, such as those of M82, NGC 1482 and NGC 253 (eg Martin 1999; Strickland et al. 2004a), are exceptional, galaxies with modest winds are widespread (Veilleux et al. 2005), as revealed by extraplanar diffuse x-ray (Fabbiano et al. 1990; Armus et al. 1995; Strickland et al. 2004b), Hα (Heckman et al. 1990; Miller & Veilleux 2003), and dust emission (Howk & Savage 1999) in several galaxies.

Interest in the physical nature of the winds and their prevalence has increased since it has been recognised they appear to play key roles in galaxy formation and the distribution of metals in the Intergalactic Medium (IGM). Both photoionization and mechanical feedback from star-forming regions have long been expected to limit star-formation on small scales (McKee & Ostriker 2007). Wind feedback has also been invoked to impede circumgalactic gas accretion and so limit the efficiency of star formation in galaxy formation models to account for disagreement between model

predictions and observations (eg Dekel & Silk 1986; Kereš et al. 2012; Keller et al. 2015; Oppenheimer & Davé 2008; Weil et al. 1998). Winds extending over hundreds of kiloparsecs may account for intergalactic metal absorption systems (see the review by Meiksin 2009).

It is widely believed galactic winds result from the collective impact of supernovae in compact star-forming regions on their surroundings (see the review by Veilleux et al. 2005). The details of the physical mechanism driving the winds, however, are still unknown. Most models are based on the injection of energy and matter by supernovae and stellar winds in a distributed region (Burke 1968; Johnson & Axford 1971; Mathews & Baker 1971; Chevalier & Clegg 1985). The most straightforward model of pressure-driven expanding gas expelled by the supernovae fails because it greatly over-predicts the gas temperature as inferred from x-ray spectra of the winds, and underpredicts the x-ray luminosities. Mass loading, in which interstellar gas is incorporated into the flow, is recognized as the most plausible explanation for the moderate temperatures and high x-ray luminosities detected (Tomisaka & Bregman 1993; Suchkov et al. 1996). This possibility receives observational support from measurements of velocity-broadened metal absorption

★ Scottish Universities Physics Alliance

line systems (Heckman et al. 2015). Sources for the mass include pre-existing interstellar gas in the vicinity of the supernovae from stellar winds, hydrodynamic ablation of gas clouds entrained in the outflow and thermal evaporation from gas clouds (Suchkov et al. 1996; Strickland & Stevens 2000; Pittard et al. 2001; Marcolini et al. 2005). Alternative wind models have also been considered, such as momentum-driven winds (Murray et al. 2005) and winds driven by cosmic ray streaming (Ipavich 1975; Uhlig et al. 2012; Girichidis et al. 2016).

Based on the stellar wind model of Castor et al. (1975) and Weaver et al. (1977) for isolated stars, the galactic superbubble model of McCray & Kafatos (1987) and Mac Low & McCray (1988) naturally incorporates mass loading sourced by thermal evaporation off the wall of the wind cavity produced by supernovae, resulting in a self-similarly expanding supershell. Analytic modelling and numerical computations suggest the initially spherically expanding superbubble soon develops into a biconal outflow within the stratified interstellar medium of a disc galaxy (Schiano 1985; Mac Low & McCray 1988; Tomisaka & Ikeuchi 1988). Asymptotically, at large distances from the galactic plane, the outflow may develop into a more spherical superwind.

A more sophisticated approach to modelling winds is to use numerical hydrodynamical computations to evolve a galactic wind from first principles, but uncertainties in the detailed structure of the interstellar medium limit the generality of the computations. The computational demands imposed by the spatial resolution necessary to capture all of the essential physics moreover precludes a fully self-consistent treatment using cosmological simulations with current resources. An element of 'sub-grid physics' is ultimately required (eg Springel & Hernquist 2003; Dalla Vecchia & Schaye 2012). Critically, all the numerical models suffer from one key deficiency: the unknown physical mechanism driving the wind. In particular, the roles of both clouds and thermal heat conduction, particularly as they affect the amount of mass loading, are unknown. While the interaction between winds and clouds has been investigated using numerical simulations (eg Cooper et al. 2008; Scannapieco & Brüggen 2015), most simulations neglect thermal heat conduction (but see D'Ercole & Brighenti 1999; Marcolini et al. 2005; Brüggen & Scannapieco 2016). The superbubble model has recently been incorporated into cosmological simulations (Keller et al. 2014), producing galaxy properties in good agreement with observations (Keller et al. 2015).

A principal goal of this paper is to derive observational means for distinguishing between models with and without thermal heat conduction. The implicit justification for neglecting heat conduction is that magnetic fields tangled by turbulence will suppress heat conductivity. On the other hand, winds will tend to comb out magnetic field lines, allowing some thermal heat conduction along the wind direction. Which of these effects dominates is not known.

The analytic modelling here is performed in the context of a homogeneous wind. The homogeneity of wind gas is currently not well constrained, although there is clear evidence for the presence of entrained gas clouds. Even if initially the gas is clumped into clouds, large mass-loading factors resulting from hydrodynamical ablation or thermal evaporation may render the hot gas interior to the wind bubble sufficiently smooth for the homogeneous models still to pro-

vide a good approximation to the wind structure. Observations suggest radiative losses, not included in the models, are generally too small to affect the energetics of the winds, although they may affect the metal column densities of embedded clouds (Heckman et al. 2001, 2002). Gravity will play a secondary role in slowing the flow, an effect not readily incorporated into an analytic treatment (but see Bustard et al. 2016), while it may limit the outflow velocity of ram-pressure driven clouds (Heckman et al. 2015). The principal role of gravity is in stratifying the galactic disc gas, as will be discussed below.

The *Chandra X-ray Observatory* has enabled the development of observing campaigns to systematically investigate the x-ray properties of star-forming galaxies (Strickland et al. 2004b; Grimes et al. 2005; Mineo et al. 2012a,b, 2014). The primary quantity focussed on in this paper is the radiative x-ray efficiency of the wind as quantified by the specific *diffuse* x-ray energy generated per solar mass of stars formed. The x-ray emission profiles extend to typical scales of several kiloparsecs (Strickland et al. 2004b; Mineo et al. 2012b), well beyond the active star-forming regions driving the outflow. Winds on these scales form bipolar cones through the stratified disc gas and become increasingly inhomogeneous due to the onset of Kelvin-Helmholtz and Rayleigh-Taylor instabilities, details not amenable to an analytic treatment. Since the diffuse x-ray profiles are strongly centrally peaked, however, the models considered here should still capture a fair fraction of the total x-ray luminosity, particularly for dwarf starbursts (Grimes et al. 2005). This paper seeks to quantify the radiative x-ray efficiency from the central region within the disc of the galaxies, allowing for a range in star-formation rates and wind properties. Although analytic models are approximate, they provide insight into the origin of observational trends in terms of the physical properties of the winds. They also provide invaluable guidance into the design and interpretation of numerical simulations.

In the next section, approximate analytic scaling relations are derived for the structure and some observational signatures of the winds. In Sec. 3, x-ray luminosity predictions are presented using full numerical integrations of the models. This is followed by predictions for radio luminosities in Sec. 4 and for metal absorption column densities in Sec. 5. The results are discussed in Sec. 6, followed by a summary of the key results in a conclusions section.

2 ANALYTIC ESTIMATES OF SPECIFIC X-RAY EMISSION

The x-ray emission from a wind arises from both thermal free-free and line emission. To understand the dependence of the emission on the properties of the sources and the surrounding gas, it is helpful first to estimate the thermal free-free component analytically. In the following section, more accurate results from numerical computations are provided including line emission. Estimates use the model of Chevalier & Clegg (1985) for a steady-state wind and of McCray & Kafatos (1987) and Mac Low & McCray (1988) for superbubbles. Both assume gravitational acceleration is negligible, a good approximation in the central regions of a galaxy where the gas is much hotter than the galactic virial

temperature. Gravity, however, produces stratification of the galactic disc gas, which results in biconal outflow. This is a limitation of both models: the steady-state wind assumes a homogeneous source, limited therefore to a region small compared with the scale-height of the disc. Comparison with numerical simulations, however, suggest the large-scale wind produced by a starburst in a cylindrical region in a disc may be rescaled to the spherically symmetric solution to high accuracy (Strickland & Heckman 2009). The superbubble model assumes a homogeneous surrounding medium. Hydro-dynamical simulations show this tends to limit the growth of the superbubble to within the disc as pressure-driven lobes emerge vertically (Mac Low et al. 1989). The analysis here concentrates on the structure of the superbubble when it reaches a size comparable to the scale-height of the disc.

2.1 Steady-state wind

The characteristic ejecta energy and mass of a core-collapse supernova are taken by Chevalier & Clegg (1985) to be $E = 10^{51}$ erg and $M = 3\,M_\odot$. Assuming a Salpeter stellar initial mass function (IMF), a lower progenitor mass limit of $8\,M_\odot$, $\nu_{\rm SN}$ for a core-collapse supernova gives a rate of about 1 core-collapse supernova per 100 solar masses of stars formed. (The value would rise by about 40 percent for a Kroupa IMF.) Characterizing the supernova rate as $0.01\nu_{100}$ supernova per solar mass of stars formed, the energy and mass injection rates for a star-formation rate $\dot{M}_*$ are $\dot{E} = (10^{49}\epsilon\,{\rm erg}\,M_\odot^{-1})\nu_{100}\dot{M}_* = \epsilon\dot{E}_1$ and $\dot{M} = (0.03\beta)\nu_{100}\dot{M}_* = \beta\dot{M}_1$, where ϵ and β allow for uncertainties in the mechanical energy and mass-loading, respectively. For $\dot{M}_*$ expressed in $M_\odot\,{\rm yr}^{-1}$, $\dot{E} = 3.17 \times 10^{41}\,{\rm erg\,s}^{-1}\,\epsilon\nu_{100}\dot{M}_*$.

Most of the bolometric thermal free-free emission originates in the central source region at $r < R$. The analytic estimate is based on emission from this region. Using the results in the Appendix for a $\gamma = 5/3$ gas, the central hydrogen density is

$$n_{\rm H0} \simeq 0.00658\,{\rm cm}^{-3}\,\frac{\beta^{3/2}}{\epsilon^{1/2}}\nu_{100}\dot{M}_* R_{100}^{-2}, \qquad (1)$$

where $\dot{M}_*$ is the star formation rate in units of $M_\odot\,{\rm yr}^{-1}$ and R_{100} is the radius of the star forming region in units of 100 pc. The central temperature is

$$T_0 = \frac{2}{5}\frac{\bar{m}}{k_{\rm B}}\frac{\epsilon}{\beta}\dot{E}_1\dot{M}_1^{-1} \simeq 4.76 \times 10^8\,{\rm K}\,\frac{\epsilon}{\beta} \simeq 14.2 v_\infty^2, \qquad (2)$$

where $\bar{m}$ is the mean mass per particle, and in the last expression the temperature is characterized by the asymptotic wind velocity at $r \gg R$,

$$v_\infty = 2^{1/2}\frac{\epsilon^{1/2}}{\beta^{1/2}}\dot{E}_1^{1/2}\dot{M}_1^{-1/2} \simeq 5790\,{\rm km\,s}^{-1}\,\frac{\epsilon^{1/2}}{\beta^{1/2}}. \qquad (3)$$

In terms of v_∞, the central hydrogen density is $n_{\rm H0} \simeq 1.28\,{\rm cm}^{-3}\,(v_\infty/1000\,{\rm km\,s}^{-1})^{-3}\epsilon\nu_{100}\dot{M}_* R_{100}^{-2}$.

Radiative cooling places a lower limit on the asymptotic wind velocity. The energy injection rate must exceed the cooling rate within the central region of the wind. The cooling rate is $n_e n_{\rm H}\Lambda_R(T)$ for electron and hydrogen number densities n_e and $n_{\rm H}$, respectively, where $\Lambda_R(T) \simeq$

$1.0 \times 10^{-22}\,{\rm erg\,cm^3\,s^{-1}}\,T_6^{-0.7}\zeta_m$ with $T_6 = T/10^6$ K and ζ_m the metallicty relative to solar (Mac Low & McCray 1988). Requiring $\dot{E} > n_e n_{\rm H}\Lambda_R(T)(4\pi R^3/3)$ imposes the robust restriction

$$v_\infty > 550\,{\rm km\,s}^{-1}\,\left(\epsilon\nu_{100}\zeta_m\dot{M}_* R_{100}^{-1}\right)^{0.14}, \qquad (4)$$

corresponding to the limit on the mass-loading factor $\beta < 110\epsilon^{0.73}(\nu_{100}\zeta_m\dot{M}_*/R_{100})^{-0.27}$. In the literature, a more commonly defined mass-loading factor is the ratio of mass outflow rate to star-formation rate. In terms of this ratio, designated here by $\beta_*(= 0.03\beta\nu_{100})$, the cooling restriction imposes

$$\beta_* = \left(\frac{1000\,{\rm km\,s}^{-1}}{v_\infty}\right)^2\epsilon\nu_{100} < 3.3\,(\epsilon\nu_{100})^{0.73}\left(\zeta_m\dot{M}_* R_{100}^{-1}\right)^{-0.27}.$$
$$(5)$$

The mass injection rate is then limited to $\dot{M} < 3.3(\epsilon\nu_{100}\dot{M}_*)^{0.73}(R_{100}/\zeta_m)^{0.27}\,M_\odot\,{\rm yr}^{-1}$. A similar restriction is derived by Zhang et al. (2014) for free-free losses alone.

As shown in the Appendix, the core density and temperature are nearly uniform within $r < 0.98R$. Approximating the density and temperature as constant within $r < R$, the total thermal free-free luminosity is

$$L_\nu^{\rm ff} \simeq 3\times 10^{16}\,{\rm erg\,s^{-1}\,Hz^{-1}}\,e^{-0.0244 e_{\rm keV}(\beta/\epsilon)}\frac{\beta^{7/2}}{\epsilon^{3/2}}(\nu_{100}\dot{M}_*)^2 R_{100}^{-1},$$
$$(6)$$

for x-rays of energy $e_{\rm keV}$ in keV. Integrating Eq. (6) over the energy band $(e_1 - e_2)$ keV, the x-ray energy produced per solar mass of stars formed is then

$$
\begin{aligned}
\frac{E_{[e_1-e_2]\,{\rm keV}}}{M_*} \simeq\ & 8 \times 10^{42}\,{\rm erg}\,M_\odot^{-1}\,\nu_{100}^2\dot{M}_* R_{100}^{-1} \\
& \times \frac{\beta^{5/2}}{\epsilon^{1/2}}\left[\exp\left(-0.0244\frac{\beta}{\epsilon}e_{1,{\rm keV}}\right)\right. \\
& \left. -\exp\left(-0.0244\frac{\beta}{\epsilon}e_{2,{\rm keV}}\right)\right].
\end{aligned}
\qquad (7)
$$

The model predicts a linear increase with the star formation rate. Taking $\epsilon = 1$ and a typical mass-loading factor of $\beta \simeq 100$, corresponding to the asymptotic wind velocity $v_\infty \simeq 600\,{\rm km\,s}^{-1}$, gives

$$\frac{E_{[0.5-2]\,{\rm keV}}}{M_*} \simeq 2 \times 10^{47}\,{\rm erg}\,M_\odot^{-1}\,\nu_{100}^2\dot{M}_* R_{100}^{-1}. \qquad (8)$$

2.2 Superbubble with thermal heat conduction

Allowing for an ambient interstellar medium and equilibration of the temperature interior to the bubble cavity by thermal heat conduction, McCray & Kafatos (1987) and Mac Low & McCray (1988) model the superbubble as a self-similar expanding stellar wind. Normalized by the typical mechanical luminosity of an OB association, $L = 10^{38}L_{38}\,{\rm erg\,s}^{-1}$, and for an ambient hydrogen density outside the wind bubble $n_{\rm H,0}$, the bubble radius increases, assuming no radiative losses, like

$$R_{\rm B} \simeq 66\,{\rm pc}\left(\frac{L_{38}t_6^3}{n_{\rm H,0}}\right)^{1/5}, \qquad (9)$$

where t_6 is the age of the bubble in units of 10^6 yr. Adopting the thermal conductivity coefficient $\kappa(T) = 6 \times$

$10^{-7} f_T T^{5/2} \, \mathrm{erg \, s^{-1} \, cm^{-1} \, K^{-7/2}}$, including a possible constant conductivity suppression factor f_T, the interior bubble temperature and ionized hydrogen number density are given in terms of the similarity variable $x = r/R_\mathrm{B}$ for radius r by

$$T \simeq (5.2 \times 10^6 \, \mathrm{K}) f_T^{-2/7} L_{38}^{8/35} n_{\mathrm{H},0}^{2/35} t_6^{-6/35} (1-x)^{2/5}, \quad (10)$$

and

$$n_\mathrm{H} \simeq (0.016 \, \mathrm{cm}^{-3}) f_T^{2/7} L_{38}^{6/35} n_{\mathrm{H},0}^{19/35} t_6^{-22/35} (1-x)^{-2/5}. \quad (11)$$

The bubble will cool primarily by line radiation at its surface. The characteristic radiative cooling time is

$$t_\mathrm{R} \simeq (15 \times 10^6 \, \mathrm{yr}) L_{38}^{3/11} n_{\mathrm{H},0}^{-8/11} f_T^{-25/22} (\zeta_m + 0.15)^{-35/22}. \quad (12)$$

The factor 0.15 has been added to ζ_m to account for hydrogen and helium cooling, where care is taken near the surface to ensure cooling is cut off below the recombination temperatures for helium and hydrogen for collisionally ionized gas, and $\Lambda_R(T) \sim T^{-1/2}$ was adopted for the surface layer, following Mac Low & McCray (1988). For high ambient hydrogen densities, cooling will limit the radius of the bubble to be smaller than the characteristic scale height of the stratified interstellar medium perpendicular to the disc. At lower densities, the bubble radius may reach the disc scale height. The wind will then evolve into a bipolar outflow perpendicular to the disc, and the expansion into the plane of the disc ceases, or may even reverse (Mac Low & McCray 1988; Mac Low et al. 1989).

Expressing the temperature and density of the gas interior to the bubble as $T = T_c u^{2/5}$ and $n_\mathrm{H} = n_{\mathrm{H}c} u^{-2/5}$, where $u = 1 - x$, the thermal free-free emission emitted by a wind bubble of radius $R_\mathrm{B} = 100 R_{\mathrm{B},100}$ pc is

$$L_\nu^\mathrm{ff} \simeq 5 \times 10^{25} \, \mathrm{erg \, s^{-1} \, Hz^{-1}} n_{\mathrm{H}c}^2 T_c^{-1/2} R_{\mathrm{B},100}^3$$
$$\times \int_0^1 \frac{du}{u} (1-u)^2 \exp\left[-\left(\frac{h_\mathrm{P} \nu}{k_\mathrm{B} T_c} \right) u^{-2/5} \right] \quad (13)$$

$$\simeq \begin{cases} 10^{26} \, \mathrm{erg \, s^{-1} \, Hz^{-1}} n_{\mathrm{H}c}^2 T_c^{-1/2} R_{\mathrm{B},100}^3 \\ \times \left[\log\left(\frac{k_\mathrm{B} T_c}{h_\mathrm{P} \nu} \right) - \frac{3+5\gamma}{5} \right] & (h_\mathrm{P} \nu \ll k_\mathrm{B} T_c); \\ 10^{27} \, \mathrm{erg \, s^{-1} \, Hz^{-1}} n_{\mathrm{H}c}^2 T_c^{-1/2} R_{\mathrm{B},100}^3 \\ \times \left(\frac{k_\mathrm{B} T_c}{h_\mathrm{P} \nu} \right)^3 e^{-h_\mathrm{P} \nu / k_\mathrm{B} T_c} & (h_\mathrm{P} \nu \gg k_\mathrm{B} T_c), \end{cases}$$

where h_P is the Planck constant, k_B is the Boltzmann constant, here $\gamma \simeq 0.5772$ is Euler's constant, and the integral has been evaluated with its asymptotic leading order behaviour retained for the two limiting cases shown. A characteristic central temperature of $\sim 4 \times 10^7$ K gives a transition energy between the two cases of about 3 keV.

At high densities, the growth of the wind bubble will be limited by cooling once the energy radiated matches the total mechanical energy deposited by the wind. This may be quantified as follows. At the cooling time $t = t_\mathrm{R}$, the central hydrogen density and gas temperature take on the values

$$n_{\mathrm{H}c} \simeq 0.003 \, \mathrm{cm}^{-3} n_{\mathrm{H},0} f_T (\zeta_m + 0.15), \quad (14)$$

independent of L_{38}, and

$$T_c \simeq 1.4 \times 10^7 \, \mathrm{K} \, (\epsilon \nu_{100} n_{\mathrm{H},0} \dot{M}_*)^{2/11} f_T^{-1/11} (\zeta_m + 0.15)^{3/11}, \quad (15)$$

respectively, where L_{38} has been converted to the star formation rate $\dot{M}_*$ ($\mathrm{M}_\odot \, \mathrm{yr}^{-1}$) using $L_{38} \simeq 3170 \epsilon \nu_{100} \dot{M}_*$ (Sec. 2.1).

The cooling radius may be expressed as

$$R_{\mathrm{B,cool}} \simeq 6.3 \, \mathrm{kpc} \, n_{\mathrm{H},0}^{-7/11} \epsilon \nu_{100} \dot{M}_*^{4/11} f_T^{-15/22} (\zeta_m + 0.15)^{-21/22}. \quad (16)$$

The corresponding bubble expansion velocity $\dot{R}_{\mathrm{B,cool}} = (3/5) R_{\mathrm{B,cool}}/t_\mathrm{R}$ at this time is

$$\dot{R}_{\mathrm{B,cool}} \simeq 27 \, \mathrm{km \, s^{-1}} \, (\epsilon \nu_{100} \dot{M}_* n_{\mathrm{H},0})^{1/11} f_T^{5/11} (\zeta_m + 0.15)^{7/11}. \quad (17)$$

The mass interior to the bubble is dominated by the evaporation off the bubble wall into the hot cavity at the rate $\dot{M}_\mathrm{ev} = (16\pi/25)[\bar{m}\kappa(T_c)/k_\mathrm{B}] R_\mathrm{B}$ (Castor et al. 1975), where $\kappa(T_C)$ is the thermal conductivity coefficient. The mass loading factor in the wind core referenced to the star formation rate becomes

$$\beta_* = \frac{\dot{M}_\mathrm{ev}}{\dot{M}_*} \simeq 2.1 \left(\dot{M}_* n_{\mathrm{H},0} \right)^{-2/11}$$
$$\times (\epsilon \nu_{100}) f_T^{1/11} (\zeta_m + 0.15)^{-3/11}. \quad (18)$$

From Eq. (13), the x-ray energy in the 0.5–2 keV band per solar mass of stars formed is then

$$\frac{E_{[0.5-2] \, \mathrm{keV}}}{M_*} \simeq 2 \times 10^{47} \, \mathrm{erg} \, M_\odot^{-1} \, (\epsilon \nu_{100})(\zeta_m + 0.15)^{-1}, \quad (19)$$

independent of the star formation rate, the ambient hydrogen density and the rate of thermal heat conduction. It corresponds to 2 percent of the mechanical energy radiated as x-rays in this band. The wind will not immediately cease as the momentum of the outflow will continue to sweep up material, but at a reduced rate (Koo & McKee 1992).

At lower densities, the bubble radius will be limited by the scale height of the gas perpendicular to the plane. The central hydrogen density and gas temperature when the bubble reaches a radius R_B are

$$n_{\mathrm{H}c} \simeq 0.23 \, \mathrm{cm}^{-3} \, (\epsilon \nu_{100})^{8/21} f_T^{2/7} n_{\mathrm{H},0}^{1/3} \dot{M}_*^{8/21} R_{\mathrm{B},100}^{-22/21} \quad (20)$$

and

$$T_c \simeq 4.6 \times 10^7 \, \mathrm{K} \, \left(\epsilon \nu_{100} \dot{M}_* / f_T R_{\mathrm{B},100} \right)^{2/7}, \quad (21)$$

respectively. The corresponding wind velocity is

$$\dot{R}_\mathrm{B} \simeq 430 \, \mathrm{km \, s^{-1}} \, \left(\epsilon \nu_{100} \dot{M}_* / n_{\mathrm{H},0} R_{\mathrm{B},100}^2 \right)^{1/3}. \quad (22)$$

The mass loading factor in the bubble is

$$\beta_* \simeq 0.64 (\epsilon \nu_{100})^{5/7} \left(R_{\mathrm{B},100} f_T / \dot{M}_* \right)^{2/7}, \quad (23)$$

independent of the ambient gas density. The x-ray energy in the 0.5–2 keV band per solar mass of stars formed is then

$$\frac{E_{[0.5-2] \, \mathrm{keV}}}{M_*} \simeq 5 \times 10^{45} \, \mathrm{erg} \, M_\odot^{-1} \, (\epsilon \nu_{100})^{13/21} f_T^{5/7}$$
$$\times n_{\mathrm{H},0}^{2/3} \dot{M}_*^{-8/21} R_{\mathrm{B},100}^{22/21}, \quad (24)$$

decreasing weakly with increasing star formation rate.

The x-ray energy produced per solar mass of stars formed may then take on a wide range of values, depending on $n_{\mathrm{H},0}$. For $n_{\mathrm{H},0} > n_{\mathrm{H},0,\mathrm{R}} \simeq 670 \, \mathrm{cm}^{-3} \, (\epsilon \nu_{100} \dot{M}_*)^{4/7} f_T^{-15/14} (\zeta_m + 0.15)^{-11/7} R_{\mathrm{B},100}$, the rate will be near $10^{47} \, \mathrm{erg} \, M_\odot^{-1}$, where it reaches a peak value independent of the ambient hydrogen density and the star formation rate once radiative cooling restricts the bubble growth.

It is instructive to compute the thermal heat conduction saturation parameter for these two limiting cases. Following Cowie & McKee (1977), a consideration of the ratio of the mean free path of the electrons to the temperature scale height for the wind, expressed as an 'inverted cloud,' shows that the surrounding density and temperature in the cloud case should be replaced by the central temperature and density of the wind. For a wind limited by radiative cooling, the saturation parameter becomes $\sigma_0 = (T_c/1.54 \times 10^7 \,\mathrm{K})^2 f_T/(n_\mathrm{Hc} R_\mathrm{B} \phi_s) \simeq (0.05/\phi_s) f_T^{1/2} (\zeta_m + 0.15)^{1/2}$, where $\phi_s \sim 1$ characterizes the uncertainty in the saturated heat flux. This is nearly identical to the value McKee & Cowie (1977) derive for interstellar clouds, below which clouds will cool and condense rather than evaporate. If the wind bubble is limited instead by the scale height of the disc to a radius $100\,\mathrm{pc}\ R_\mathrm{B,100}$, the saturation parameter becomes $\sigma_0 \simeq (0.39/\phi_s) f_T^{1/7} (\epsilon \nu_{100} \dot{M}_*)^{4/21} n_\mathrm{H,0}^{-1/3} R_\mathrm{B,100}^{-11/21}$. Thermal heat conduction is thus close to being saturated ($\sigma_0 > 1$) for typical values of the parameters. Only models with $\sigma_0 < 1$ are considered here so that the classical heat conduction description applies.

In the following section, more precise numerical predictions are made for the models, including the contribution from metal emission lines. Comparisons with observations are also drawn.

3 NUMERICAL EVALUATION OF SPECIFIC X-RAY EMISSION

3.1 Data and modelling

The high angular and spectral resolution of the *Chandra X-ray Observatory* have enabled quantification of the correlation between the soft x-ray diffuse emission associated with star forming regions within galaxies and the star formation rate. From measurements of 6 disc galaxies, Owen & Warwick (2009) find $L_{[0.3-1]\,\mathrm{keV}} \simeq (2-10) \times 10^{38} \,\mathrm{erg\,s^{-1}} \dot{M}_* \,(\mathrm{M_\odot\,yr^{-1}})$. Only the most luminous point sources were removed, so that their value may be conservatively viewed as an upper limit to the x-ray luminosity of a gas component. Li & Wang (2013) find a similar correlation between diffuse galactic coronal emission, corrected for observed or estimated stellar contributions, and the star formation rate of $L_{[0.5-2]\,\mathrm{keV}} \simeq 1.4^{+1.1}_{-0.8} \times 10^{39} \,\mathrm{erg\,s^{-1}} \dot{M}_* \,(\mathrm{M_\odot\,yr^{-1}})$ for 53 nearby disc galaxies. Based on star formation rate estimates from infra-red and UV measurements restricted to the same projected region as the diffuse x-ray emission, in a sample of galaxies cleaned of those showing evidence of an active nucleus and with detected or the estimated contribution of unresolved high mass x-ray binaries removed, Mineo et al. (2012b) obtained $L_{[0.5-2]\,\mathrm{keV}} \simeq (8.3 \pm 0.1) \times 10^{38} \,\mathrm{erg\,s^{-1}} \dot{M}_* \,(\mathrm{M_\odot\,yr^{-1}})$ for a sample of 21 late-type galaxies. (A Salpeter stellar initial mass function was assumed.) On fitting a two-component thermal model to the spectra, they find a correlation between the gaseous contribution to the diffuse x-ray luminosity and the star formation rate of

$$L_{[0.5-2]\,\mathrm{keV}} \simeq (5.2 \pm 0.2) \times 10^{38} \,\mathrm{erg\,s^{-1}} \dot{M}_* \,(\mathrm{M_\odot\,yr^{-1}}), \quad (25)$$

or $E_{[0.5-2]\,\mathrm{keV}}/M_* \simeq (1.6 \pm 0.1) \times 10^{46} \,\mathrm{erg\,M_*^{-1}}$. For 9 galaxies, they find spectral evidence for substantial absorption internal to the galaxies. Using these systems, they estimate the *intrinsic* diffuse gaseous emission to be

$$L_{[0.3-10]\,\mathrm{keV}} \simeq (7.3 \pm 1.3) \times 10^{39} \,\mathrm{erg\,s^{-1}} \dot{M}_* \,(\mathrm{M_\odot\,yr^{-1}}), \quad (26)$$

or $E_{[0.3-10]\,\mathrm{keV}}/M_* \simeq (2.3 \pm 0.4) \times 10^{47} \,\mathrm{erg\,M_*^{-1}}$.

Since the x-ray emission in the wind models peaks within the energy bands used to measure the emission, a more precise comparison between the models and the measurements requires evaluating the predicted luminosities by numerically integrating the emission over the full density and temperature profiles of the models. In addition to thermal free-free, x-ray line emission also contributes substantially to the overall x-ray budget. The CHIANTI rates (Landi et al. 2012) for collisionally ionized gas are adopted from Cloudy (13.03) (Ferland et al. 2013), and emission tables for solar and half-solar metallicity computed. Numerical integrations of the models interpolate on the tables. Comparisons with measurements are made separately below for the steady-state wind model and the superbubble model.

3.2 Steady-state wind

The specific x-ray emission in the bands $0.5-2\,\mathrm{keV}$ and $0.3-10\,\mathrm{keV}$ for the steady-state wind model is shown in Fig. 1 as a function of star formation rate. A source region of radius $R = 100$ pc is adopted, with solar metallicity. Emission from outside the source region is included, although it diminishes rapidly with distance outward. The mass-loading factor is expressed in terms of the asymptotic wind velocity v_∞.

The specific emissivity is a decreasing function of v_∞. Expanding the source region to $R = 200$ pc is found to decrease the emission in the $0.5 - 2$ keV band by about 30 percent, the same trend, but with a somewhat weaker dependence, as predicted by Eq. (7). The x-ray emission is diminished by 30–50 percent on going from solar to half-solar metallicity for $v_\infty > 500\,\mathrm{km\,s^{-1}}$.

In the broader energy band $0.3 - 10$ keV, the specific emissivity, shown in the right panel of Fig. 1, decreases with increasing volume of the source region, varying nearly as rapidly as $1/R$, as in Eq. (7). The specific emissivity varies nearly linearly with metallicity, except for $v_\infty \gtrsim 1000\,\mathrm{km\,s^{-1}}$, for which the specific emissivity depends only weakly on the metallicity.

The predicted linearly increasing trend with star formation rate is not consistent with the observations. The data from Mineo et al. (2012b) suggests a constant amount of x-ray energy emitted per unit mass of star formed. In the energy band $0.5 - 2$ keV, this is matched by allowing a tight correlation between the asymptotic wind velocity and the star formation rate according to $v_\infty \simeq 1000 \dot{M}_*^{1/6} \,\mathrm{km\,s^{-1}}$, corresponding to a central hydrogen density $n_\mathrm{H,0} \simeq 1.3 \dot{M}_*^{1/2} \,\mathrm{cm^{-3}}$. This results in an increasing amount of mass loading for a decreasing star formation rate, a general requirement recognized by Zhang et al. (2014).

Results for galaxies corrected for internal absorption are shown in the right hand panel of Fig. 1 for the band $0.3 - 10$ keV. The near constancy of the specific emissivity with star formation rate persists in the data. Agreement with the data may again be achieved if the wind velocity were tightly correlated with the star formation rate according to $v_\infty \simeq 700 \,\mathrm{km\,s^{-1}} \dot{M}_*^{1/6}$, corresponding to a
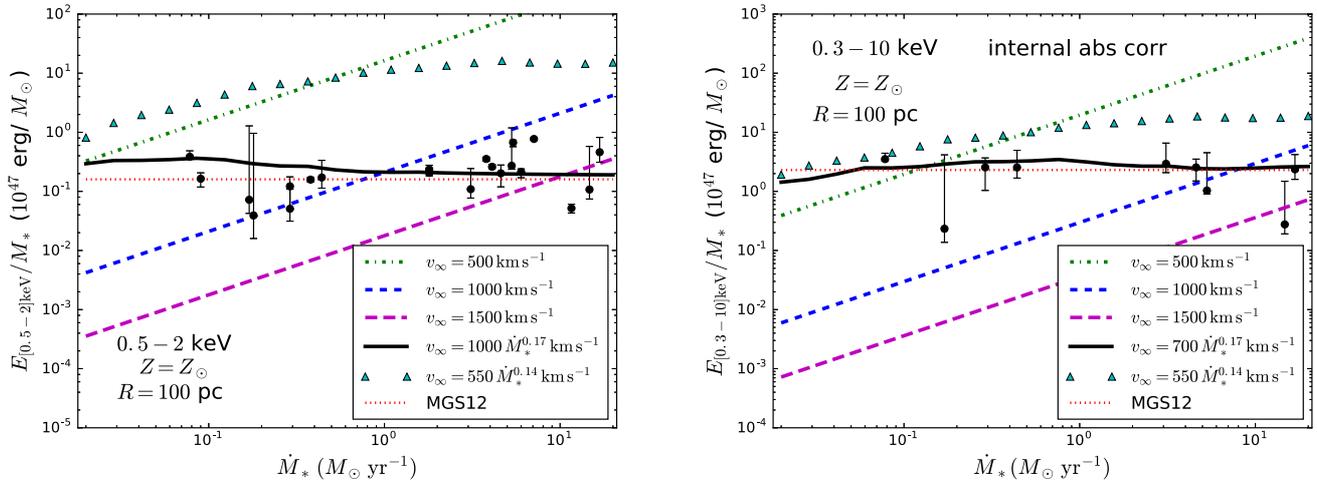
Figure 1. X-ray emission per solar mass of stars formed for a steady-state wind. Left panel: Shown for the x-ray band $0.5 - 2$ keV as a function of the star formation rate, for asymptotic wind velocities $v_\infty = 500$, 1000 and 1500 km s^{-1}. The data points are from Mineo et al. (2012b). The error bars represent uncertainties in the distances to the galaxies. Right panel: As in the left panel, but for the x-ray band $0.3 - 10$ keV. The data points are from Mineo et al. (2012b), including correction for internal absorption. The triangles indicate the upper bound imposed by radiative cooling (see text). A source region 100 pc in radius and solar metallicity are assumed for both panels.

central hydrogen density $n_{\rm H,0} \simeq 4\dot{M}_*^{1/2}\,{\rm cm}^{-3}$. The scaling with star formation rate is bracketed by that expected from Eqs. (6) and (7), which give for a constant luminosity per rate of star formation the approximate analytic scaling $v_\infty \sim (\epsilon^2 \nu_{100}^2 \dot{M}_*/R_{100})^\alpha$ with $\alpha = 1/7 - 1/5$. The velocity correlations are close to the cooling restriction Eq. (4), suggesting a narrow range is allowed for viable winds (cf Zhang et al. 2014).

3.3 Superbubble with thermal heat conduction

Allowing for thermal evaporation from a surrounding medium results in a much narrower range in specific emissivity compared with the steady state model. Results assuming a maximum radius of 100 pc for the expanding bubble and for solar metallicity are shown in Fig. 2. The results shown are time-averaged over the duration of the spherical expansion of the wind, assumed to cease at the cooling time, Eq. (12), or when it reaches the maximum radius. X-ray emission only from within the maximum radius is computed. The emission will fall off rapidly away from the plane if the superbubble expands out of the disc, but emission from an extended region may be comparable to that from within the disc. A multi-dimensional model is required to estimate the full emission more accurately.

The specific x-ray emissivity increases with the ambient hydrogen density approximately as $n_{\rm H,0}^{0.7}$, in agreement with Eq. (24), except at the highest density and low star formation rate where the wind expansion is cooling limited. At high densities, the specific emissivity becomes nearly independent of the star formation rate and gas density, in agreement with Eq. (19).

For low star formation rates and low ambient hydrogen densities, the specific emissivity nearly halves on going from solar to half-solar metallicity. The x-ray emission is dominated by line emission. The difference is much more moder-

ate at high star formation rates and high ambient densities, for which line emission no longer dominates. At low ambient hydrogen densities, the specific emissivity increases linearly with the maximum bubble radius, but less rapidly at higher densities as cooling becomes important, especially for low star formation rates, in accordance with Eqs. (19) and (24).

As shown in the left hand panel of Fig. 2, comparison with the measured specific emissivities using the data from Mineo et al. (2012b), assuming no internal absorption from the galaxies, shows good agreement for ambient gas densities of $n_{\rm H,0} \simeq 1 - 10\,{\rm cm}^{-3}$. For a fixed star formation rate, the required $n_{\rm H,0}$ will scale like $R_{\rm B}^{-11/7}$ according to Eq. (24). Since the measured values likely exceed the emission from the inner region within the disc by a factor of a few, the implied hydrogen densities are likely somewhat smaller. Allowing for internal absorption, agreement with the data in the right hand panel shows values of $n_{\rm H,0} \simeq 10 - 100\,{\rm cm}^{-3}$ are preferred. No other parameters need be adjusted: the model predicts the specific x-ray emissivity is only weakly dependent on the star formation rate, in agreement with the data.

4 SPECIFIC RADIO EMISSION

4.1 Data and modelling

The radio continuum radiation emitted by star-forming galaxies scales with the star formation rate, at least for large radio luminosities (Condon 1992; Bell 2003). The physical origin of the emission is unknown, but it is suspected to arise both from shocks driven by stellar winds and supernovae and from cosmic rays in a large-scale magnetic field. Measurements suggest that 90 percent of the continuum emission at 1.4 GHz is synchrotron and 10 percent thermal free-free in nature, suggesting a component from H ɪɪ regions as well (Condon 1992). Modelling all these effects is well beyond the
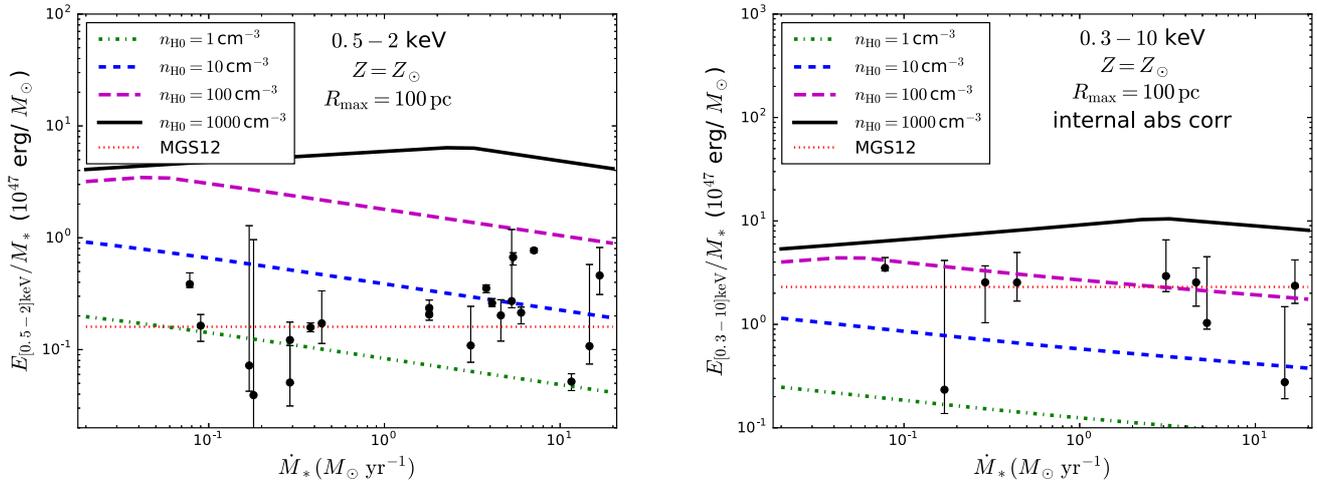
Figure 2. X-ray emission per solar mass of stars formed for a superbubble including thermal heat conduction. Left panel: Shown for the x-ray band $0.5 - 2$ keV as a function of the star formation rate, for external hydrogen densities $n_{\mathrm{H,0}} = 1, 10, 100$ and 1000 cm s^{-3}. The data points are from Mineo et al. (2012b). Right panel: As in the left panel, but for the x-ray band $0.3 - 10$ keV. The data points are from Mineo et al. (2012b), including correction for internal absorption. The error bars represent uncertainties in the distances to the galaxies. A maximum wind radius of 100 pc and solar metallicity are assumed for both panels.

scope of this paper. Here only the synchrotron and free-free diffuse radio emission from the wind regions are estimated. (Additional emission will arise from compact radio sources associated with any recent supernovae.) In comparing with radio data, it is unclear from which scale to take the emission. The correlation between the radio continuum and the star formation rate is based on extended regions that likely include emission from large-scale interstellar cosmic rays. A representative value is

$$L_{1.4\,\mathrm{GHz}}(\mathrm{erg\,s^{-1}\,Hz^{-1}}) \simeq 8.4 \times 10^{27} \dot{M}_* \, (\mathrm{M_\odot\,yr^{-1}}) \quad (27)$$

(Condon et al. 2002). By contrast, the dominant emission from shocks within the wind region would be much more centrally concentrated.

The *FIRST* radio survey (Becker et al. 1995) includes data that matches the scale of the x-ray and star-forming regions, typically up to a few arcminutes, measured by Mineo et al. (2012b). We compare the models with two 1.4 MHz continuum measurements from the *FIRST* survey, the large-scale value centred on each galaxy and the brightest unresolved peak value in the nucleus of the galaxy, corresponding typically to a region within the central 100–500 pc of the galaxy for a source at a distance of 10–20 Mpc. As shown below, the large scale values agree well with Eq. (27), corresponding to $L_{1.4\,\mathrm{GHz}}/\dot{M}_* \simeq 2.6 \times 10^{35} \, \mathrm{erg\,Hz^{-1}\,M_\odot^{-1}}$.

The synchrotron and thermal free-free emission are computed for the models as in Meiksin & Whalen (2013). In brief, a power-law energy distribution $dn/d\epsilon \sim \epsilon^{-p_e}$ is assumed for the relativistic electrons, with an energy density a fraction f_e of the local thermal energy density. The magnetic field energy density is also taken to be f_e for simplicity, corresponding to approximate equipartition. The relativistic electrons are allowed to cool by synchrotron and thermal free-free radiation and by excitation of plasmon waves following the passage of the wind-driven shock front into the interstellar gas. Thermal free-free and synchrotron self-absorption are included, although for the frequencies of in-

terest these are generally negligible in the models considered. Observations of supernova remnant spectra suggest typical values for the relativistic electron energy index of $2 < p_e < 3$ (Chevalier 1998; Weiler et al. 1986), while representative model values for the relativistic electron energy density fraction range over $0.001 < f_e < 0.2$ (Chevalier et al. 2006). The predictions of the wind models for radio emission are estimated to check they do not exceed the observed limits for plausible parameters. Virtually all the emission predicted by the models is synchrotron radiation; the thermal free-free component is two to three orders of magnitude smaller.

4.2 Steady-state wind

The x-ray measurements require models with mass-loading from a gas reservoir surrounding the supernovae. The wind will then drive a shock into the surroundings, producing relativistic electrons. An estimate of the expected synchrotron emission may be made adopting a characteristic wind age of $10^7 t_{w,7}$ yr.

For low star formation rates the synchrotron emission is dominated by the source region $r < R$, giving, for $p_e = 2$,

$$\frac{S_{1.4\mathrm{GHz}}}{\dot{M}_*} \simeq 5 \times 10^{37} \, \mathrm{erg\,Hz^{-1}\,M_\odot^{-1}} \, \nu_{\mathrm{GHz}}^{-1/2} f_e^{7/4} R_{100}^{-1/2}$$

$$\times \left(\frac{1000\,\mathrm{km\,s^{-1}}}{v_\infty} \right)^{7/4} (\epsilon\nu_{100})^{7/4} \dot{M}_*^{3/4}. \quad (28)$$

For a typical value $f_e = 0.01$, $S_{1.4\,\mathrm{GHz}}/\dot{M}_* \simeq 1.2 \times 10^{34} \, \mathrm{erg\,Hz^{-1}\,M_\odot^{-1}}$.

At higher star formation rates, the density becomes sufficiently high that two additional effects become important: synchrotron and plasmon generation losses deplete the central region of relativistic electrons; for sufficiently strong synchrotron losses the critical frequency falls to several gigahertz or less. Emission then arises only from outside the
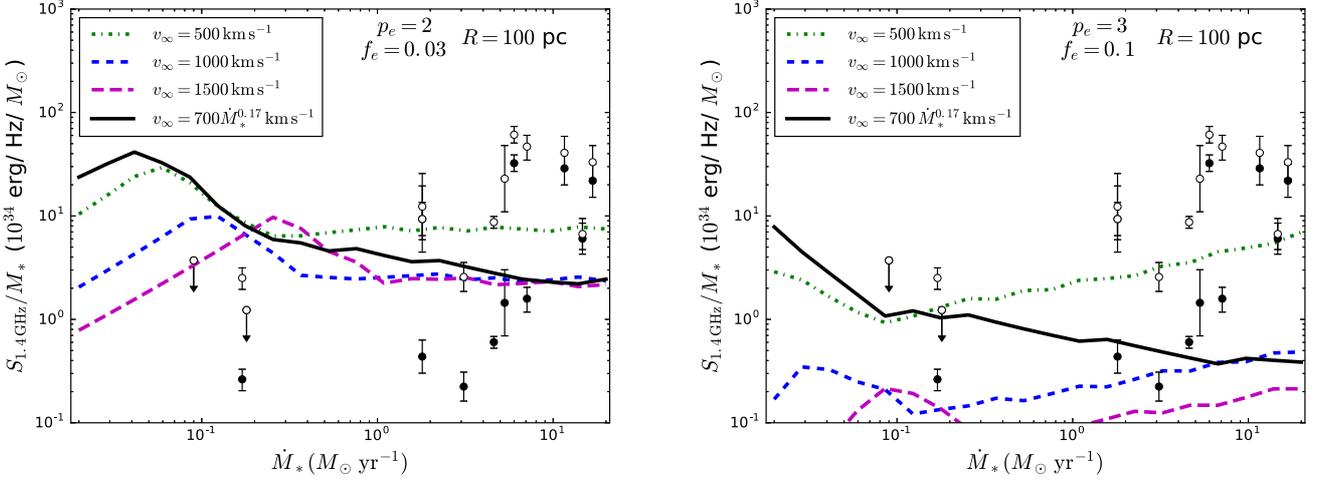
Figure 3. Radio continuum emission at 1.4 GHz per solar mass of stars formed for a steady-state wind. Shown for a relativistic electron energy index $p_e = 2$ and energy density fraction $f_e = 0.03$ (left panel) and $p_e = 3$, $f_e = 0.1$ (right panel), as a function of the star formation rate, for asymptotic wind velocities $v_\infty = 500$, 1000 and 1500 km s^{-1}. The emission adopting $v_\infty = 700\dot{M}_*^{1/6}$ km s^{-1} is shown by the solid (black) lines. The data points are from the *FIRST* radio survey. The error bars represent distance uncertainties. Open points represent the large-scale emission; filled points represent the peak unresolved emission (see text). A wind source region 100 pc in radius is assumed for both panels.

source region. The criterion for plasmon and synchrotron losses not to deplete the population of relativistic electrons is $f_e n_{\rm H} P t_{w,7}^2 < 8 \times 10^{-11}$ dyne cm^{-5}, where P is the gas pressure in the wind[1]. Using the asymptotic limits for density and pressure, this requires emission to arise only from radii

$$\frac{r}{R} > 1.1 f_e^{3/16} R_{100}^{-3/4} t_{w,7}^{3/8} \left(\epsilon \nu_{100} \dot{M}_*\right)^{3/8} \left(\frac{1000\,{\rm km\,s^{-1}}}{v_\infty}\right)^{3/4}, \tag{29}$$

corresponding to a maximum characteristic hydrogen number density of about $0.3 n_{\rm H0}$. The resulting rate of radio energy generation at frequency $10^9 \nu_{\rm GHz}$ Hz per solar mass of stars formed is

$$\frac{S_\nu}{\dot{M}_*} \simeq 4 \times 10^{37}\,{\rm erg\,Hz^{-1}\,M_\odot^{-1}}\,\nu_{\rm GHz}^{-1/2} f_e^{39/32} R_{100}^{13/8}$$
$$\times \left(\frac{v_\infty}{1000\,{\rm km\,s^{-1}}}\right)^{3/8} (\epsilon \nu_{100})^{11/16} \dot{M}_*^{-5/16} t_{w,7}^{-17/16}. \tag{30}$$

At even higher densities, once synchrotron losses lower the synchrotron critical frequency into the gigahertz range, emission above frequency $\nu_{\rm GHz}$ occurs only at radii

$$\frac{r}{R} > 3.2 \nu_{\rm GHz}^{1/5} f_e^{3/10} R_{100}^{1/5} t_{w,7}^{2/5} \left(\epsilon \nu_{100} \dot{M}_*\right)^{3/10} \left(\frac{1000\,{\rm km\,s^{-1}}}{v_\infty}\right)^{3/10}, \tag{31}$$

resulting in a rate of radio energy generation per solar mass

of stars formed of

$$\frac{S_\nu}{\dot{M}_*} \simeq 3 \times 10^{35}\,{\rm erg\,Hz^{-1}\,M_\odot^{-1}}\,\nu_{\rm GHz}^{-16/15} f_e^{9/10} R_{100}^{-16/15}$$
$$\times \left(\frac{1000\,{\rm km\,s^{-1}}}{v_\infty}\right)^{9/10} (\epsilon \nu_{100})^{9/10} \dot{M}_*^{-1/10} t_{w,7}^{-17/15}. \tag{32}$$

Results from numerically integrating the model are shown in Fig. 3. Since the wind is in a steady state, the time since the shock passed a given radius is undetermined in the model. To allow an estimate of the synchrotron emission, the wind has been arbitrarily assumed to have reached a distance of 10 kpc from the source region, corresponding to an age of $t_{\rm age} = 10\,{\rm kpc}/v_\infty$. The 1.4 GHz emission is displayed as a function of the star-formation rate and v_∞ for $p_e = 2$, $f_e = 0.03$ and $p_e = 3$, $f_e = 0.1$. All three trends with the star formation rate are apparent: a rise ($\dot{M}_*^{3/4}$), followed by a decline ($\dot{M}_*^{-5/16}$) once synchrotron and plasmon losses pinch off the relativistic electron distribution within the wind source region, and finally a near constant level ($\dot{M}_*^{-1/10}$) once synchrotron losses restrict the generation of 1.4 GHz power to regions well outside the core. (The power at large star formation rates for the $v_\infty = 1500$ km s^{-1} case differs from the trend with v_∞ in Eq. (32) because the radius at which the critical frequency exceeds 1.4 GHz lies just outside the source region, where the asymptotic decrease of pressure with radius is no longer a good approximation.) For a high star formation rate, the radio spectrum for $p_e = 2$ is found to steepen to $\nu^{-\alpha_S}$ with $\alpha_S \simeq 1.5$, rather than the expected $\alpha_S = (p_e - 1)/2 = 1/2$, as is found for low star formation rates: the truncation of the emitting volume at high densities steepens the spectrum.

The predicted trend adopting the correlation $v_\infty \simeq 700$ km s^{-1} $\dot{M}_*^{1/6}$ is shown by the solid (black) curves. For $p_e = 2$, the fluxes for the unresolved radio sources are largely recovered or exceeded. The high flux values for the highest star-formation rates are matched only for $f_e \simeq 0.1 - 0.2$, the

---

[1] The constraint follows from equations (B3) and (B6) in Meiksin & Whalen (2013), giving a lower limit on the relativistic boost factor of the electrons of $\gamma_l \simeq 870 n_{\rm H} t_{w,7}$ with a plasmon excitation energy loss timescale exceeding $10^7 t_{w,7}$ yrs and an upper limit of $\gamma_u \simeq 6.5 \times 10^{-8}/f_e P t_{w,7}$ to avoid synchrotron energy losses over this timescale. Requiring $\gamma_l < \gamma_u$ yields the relation in the text.

limiting values inferred for supernova remnants. These high fluxes, however, are derived from distant galaxies within regions unresolved on the scales of 1–2 kpc, so the radio emission may be contaminated by emission from cosmic rays interacting with large-scale galactic magnetic fields. The predicted excess emission for unresolved sources with low flux values may indicate a reduced volume filling factor of emitting electrons, resulting in small volume-averaged values for the relativistic energy fraction. At high star formation rates, the radio flux also decreases inversely with the bubble size, according to Eq. (32). Alternatively, the relativistic electron energy distribution may be steeper. For $p_e = 3$, $f_e \approx 0.1$ recovers the lower flux values of the unresolved sources.

4.3 Superbubble with thermal heat conduction

For the superbubble model, the characteristic radio emission for a scale-height limited superbubble from within $R_{B,100}$ is given approximately by

$$\frac{S_\nu}{\dot{M}_*} \simeq 1.0 \times 10^{38} \, \mathrm{erg\,Hz^{-1}\,M_\odot^{-1}} \, \nu_{\mathrm{GHz}}^{-1/2} f_e^{7/4}$$
$$\times (\epsilon\nu_{100})^{7/6} n_{\mathrm{H},0}^{7/12} \dot{M}_*^{1/6} R_{\mathrm{B},100}^{2/3}, \quad (33)$$

nearly independent of the star formation rate. The radio emission is independent of any suppression of thermal conductivity since the radio power is determined by the thermal energy density, not the gas density or temperature separately in the absence of significant attenuation. Results from numerical integration of the wind equations are shown in Fig. 4. The bubble region recovers the full range of measured large-scale radio power for $p_e = 2$ and $f_e = 0.01$. The larger flux values, at high star formation rates, require a high ambient hydrogen density of $n_{\mathrm{H},0} \sim 100 \, \mathrm{cm}^{-3}$, the upper value required by the x-ray data. The lower power from unresolved regions is over-predicted for the higher star formation rates, possibly indicating a reduced volume filling factor of emitting electrons. The steeper electron distribution case with $p_e = 3$ requires increasing the relativistic electron energy fraction to $f_e = 0.1$, approaching the limit from supernova remnant modelling. A near constant specific radio power is found for a given ambient hydrogen density, only weakly dependent on the star formation rate, in agreement with Eq. (33).

5 METAL COLUMN DENSITIES

5.1 Data and modelling

An estimate of the column densities of metal ions within the winds may be made as follows. For solar metallicity, abundances by number of commonly detected metal atoms compared with hydrogen include: $\log_{10}\xi_{\mathrm{He}} = -1.07$, $\log_{10}\xi_{\mathrm{C}} = -3.57$, $\log_{10}\xi_{\mathrm{N}} = -4.17$, $\log_{10}\xi_{\mathrm{O}} = -3.31$, $\log_{10}\xi_{\mathrm{Si}} = -4.49$ and $\log_{10}\xi_{\mathrm{S}} = -4.88$ (Asplund et al. 2009). Any given ionization state will dominate at a particular temperature where it contributes most to the column density of that ion, although for some species neighbouring ionization states share substantially in the ionization. Temperatures at which commonly measured ions peak include: C III at $10^{4.8}$ K ($10^{-3.6}$), C IV at $10^{5.0}$ K ($10^{-4.1}$), N II at $10^{4.4}$ K ($10^{-4.2}$), N III at $10^{4.9}$ K ($10^{-4.2}$), O VI at $10^{5.5}$ K

$(10^{-4.2})$, Si III at $10^{4.5}$ K ($10^{-4.6}$), Si IV at $10^{4.8}$ K ($10^{-5.0}$), SIII at $10^{4.7}$ K ($10^{-5.0}$) and S IV at $10^{5.0}$ K ($10^{-5.1}$), where the peak abundance fractions by number relative to hydrogen, $\xi_{i,\mathrm{max}}$, are indicated in parentheses. It is noted these values will be modified if the gas is not in collisional ionization equilibrium, as appears to be the case for some high velocity clouds in the Galactic halo (Shull et al. 2011).

For the steady-state wind model with $v_\infty > 500 \, \mathrm{km\,s^{-1}}$ and wind core radius $R = 100$ pc, the temperatures at which these ion abundances peak are achieved only outside the core, where the gas density is rapidly declining. The column density of a typical ion like C III is negligibly small in the core, $N_{\mathrm{CIII}} \simeq 10^7 \, \mathrm{cm}^{-2}$. Of the ions listed above, only O VI would achieve a measurable column density within the core, $N_{\mathrm{OVI}} \simeq 10^{14} \, \mathrm{cm}^{-2}$. It is noted, however, that at the interface of the wind shock and the interstellar medium in the galactic disc, detectable levels of absorption may arise (Dopita & Sutherland 1996). Such systems could possibly be distinguished from those produced by superbubbles, discussed below, through their kinematics.

For $r \gg R$, the wind temperature is $T \simeq 6.7v_\infty^2(R/r)^{4/3}$. For a given ion i, the radius and density at which $T = T_{\mathrm{max}} = 10^5 \, \mathrm{K} \, T_{\mathrm{max},5}$ are $r_{\mathrm{max}} \simeq 23RT_{\mathrm{max},5}^{-3/4}(v_\infty/1000 \, \mathrm{km\,s^{-1}})^{3/2}$ and $n_{\mathrm{H,max}} \simeq 4.4 \times 10^{-4} \, \mathrm{cm}^{-3} T_{\mathrm{max},5}^{3/2}(v_\infty/1000 \, \mathrm{km\,s^{-1}})^{-6}\epsilon\nu_{100}\dot{M}_*R_{100}^{-2}$. The corresponding column density will be

$$N_i \simeq n_{\mathrm{H,max}} r_{\mathrm{max}} \xi_{i,\mathrm{max}}$$
$$\simeq 5.7 \times 10^{14} \, \mathrm{cm}^{-2} \epsilon\nu_{100}\dot{M}_* R_{100}^{-1} \left(\frac{1000 \, \mathrm{km\,s^{-1}}}{v_\infty}\right)^{9/2}$$
$$\times \left(\xi_{i,\mathrm{max}} T_{\mathrm{max}}^{3/4}\right). \quad (34)$$

The column densities decline very rapidly with v_∞. Representative values for some common ions, computed numerically by integrating along the full wind solution at $r > R$, are shown in Fig. 5 (left panel). These represent the maximum column densities that would arise from the homogeneous wind for lines of site passing through the region $r \simeq r_{\mathrm{max}}$. At larger distances, the column densities will rapidly decline.

In the superbubble model, the column densities are dominated by absorption from a very thin layer at the bubble interface with the interstellar medium. For the scale-height limited case with a bubble radius R_B, the characteristic temperature scale height at the position where $T = T_{\mathrm{max}}$ for a given ion is $L_T = |dr/d\log T|_{\mathrm{max}} = (5/2)R_B(T_{\mathrm{max}}/T_c)^{5/2} \simeq 5.5 \times 10^{-7} R_B(f_T R_{B,100}/\epsilon\nu_{100}\dot{M}_*)^{5/7}T_{\mathrm{max},5}^{5/2}$, corresponding to a hydrogen density $n_{\mathrm{H,max}} \simeq 110 \, \mathrm{cm}^{-3} \, n_{\mathrm{H},0}^{1/3}\epsilon\nu_{100}\dot{M}_*^{2/3}R_{B,100}^{-4/3}T_{\mathrm{max},5}^{-1}$. The column density of ion i is then

$$N_i \simeq n_{\mathrm{H,max}}\xi_{i,\mathrm{max}} L_T$$
$$\simeq 5.7 \times 10^8 \, \mathrm{cm}^{-2} \, n_{\mathrm{H},0}^{1/3}(\epsilon\nu_{100}\dot{M}_*)^{-1/21}R_{B,100}^{8/21}f_T^{5/7}$$
$$\times \left(\xi_{i,\mathrm{max}} T_{\mathrm{max}}^{3/2}\right), \quad (35)$$

nearly independent of the star formation rate and only weakly sensitive to the ambient gas density and size of the bubble. Representative values, computed numerically by integrating through the centre of the region $r < R_B$, are shown in Fig. 5 (right panel). This is a minimal value that must arise in the thermal conductive interface with the interstel-
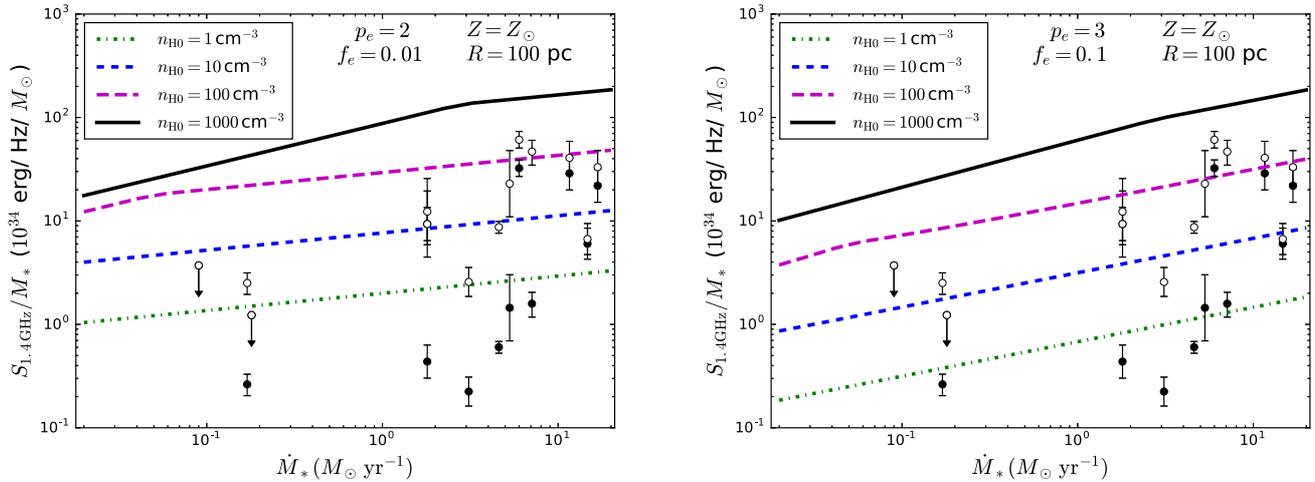
Figure 4. Radio continuum emission at 1.4 GHz per solar mass of stars formed for the superbubble model. Shown for relativistic electron distribution index $p_e = 2$ and energy density fraction $f_e = 0.01$ (left panel) and $p_e = 3$, $f_e = 0.1$ (right panel), as a function of the star formation rate, for external hydrogen densities $n_{H,0} = 1$, 10, 100 and 1000 cm s^{-3}. The data points are from the *FIRST* radio survey. Open points represent the large-scale emission; filled points represent the peak unresolved emission (see text). A maximum bubble radius of 100 pc is adopted and solar metallicity.
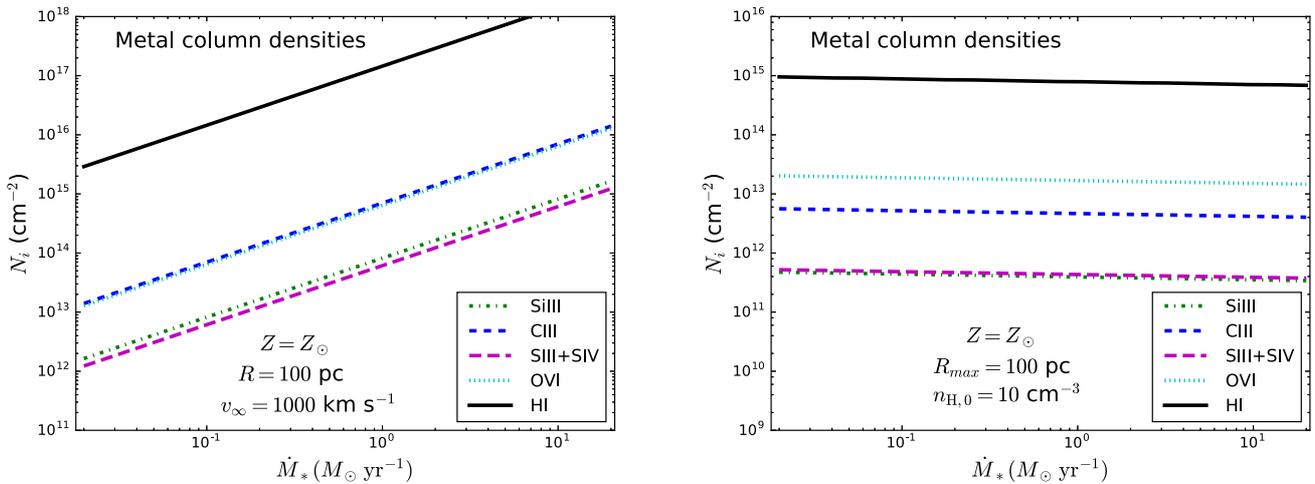

Figure 5. Column densities for selected metal ions, shown for the steady state model for $v_\infty = 1000 \, \mathrm{km \, s^{-1}}$ (left panel) and the superbubble model for $n_{H,0} = 10 \, \mathrm{cm^{-3}}$ (right panel). Also shown is the H I column density. A source region of 100 pc radius is adopted for the steady state model, and a maximum bubble radius of 100 pc for the superbubble model. Solar metallicity is assumed for both.

lar medium. Substantially lower values would be evidence against the superbubble model. The column density for H I is also a minimal value, and it will generally be small compared with the H I column density through the surrounding disc.

6 DISCUSSION

6.1 X-ray constraints

Both the freely expanding steady-state wind model and the self-similarly expanding superbubble model with thermal heat conduction may account for the measured amount of diffuse soft x-ray energy generated per unit mass in

stars formed. An additional assumption of a tight correlation between the asymptotic wind velocity and the star formation rate, however, is required for the steady state model. By contrast, thermal evaporation from the cavity walls in the superbubble model naturally accounts for the measured amount of difuse x-ray energy per unit mass in stars formed for characteristic interstellar gas densities $1 < n_{H,0} < 100 \, \mathrm{cm^{-3}}$, with the higher values favoured if much of the soft x-ray emission is absorbed internally to the galaxies.

In the steady state model, the required correlation between the asymptotic wind velocity and the star formation rate, particularly for the high x-ray luminosities when internal galactic absorption is allowed for, is close to the mini-
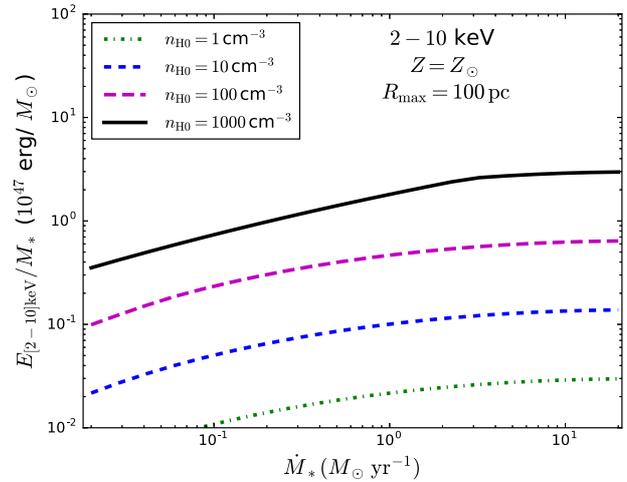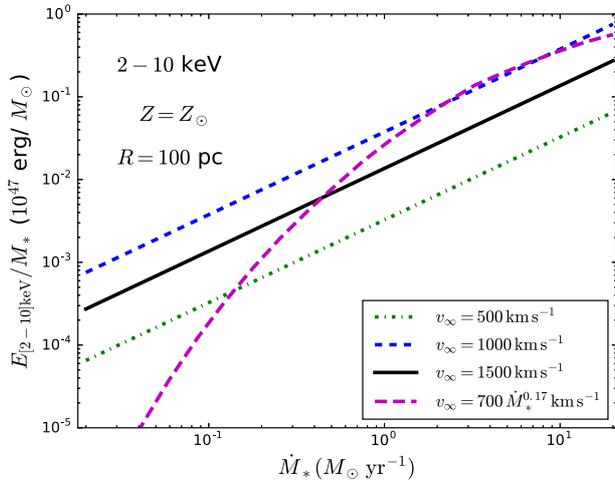
Figure 6. X-ray emission in the 2–10 keV band per solar mass of stars formed for a steady-state wind (left panel) and for a superbubble (right panel), both as a function of the star formation rate. A source region of 100 pc radius is adopted for the steady state model, and a maximum wind radius of 100 pc for the superbubble. Solar metallicity is assumed for both models.

mum wind velocity (Eq. [4]) for which a steady-state wind may be maintained against radiative cooling within the star-forming region, consistent with the narrow range in observed radiative efficiencies. But it does not provide a reason for the narrow range. One possibility is that the winds are driven by superbubbles. Once a superbubble expands to the scale-height of the galactic disc, its thermal pressure drives a vertical conical outflow rather than further expansion into the disc (Schiano 1985; Mac Low & McCray 1988). Simulations suggest the outflow is nearly adiabatic (Keller et al. 2015), so that it may be approximated by the steady state model with a superbubble as the source. The rate of mechanical energy injected by supernovae and the rate of evaporative mass loss from the disc may be used to define an effective asymptotic wind velocity for the superbubble:

$$v_\infty^{\rm eff} = \left(\frac{2\dot{E}}{\dot{M}_{\rm ev}}\right)^{1/2} = 850 \text{ km s}^{-1} \left(\epsilon\nu_{100}\dot{M}_*/f_T R_{\rm B,100}\right)^{1/7}, \quad (36)$$

close to the required relation found for the steady-state wind solution. This may reconcile the two models: thermal heat conduction sets the source terms that initiate the wind, which then 'blows out' vertically into a steady-state outflow (Mac Low et al. 1989; Mac Low & Ferrara 1999; Fujita et al. 2003, 2004; Keller et al. 2014).

For a bubble to blow out, two criteria must be satisfied: the cooling radius must exceed the disc scale height and the bubble velocity must exceed the sound speed in the surrounding medium. Both of these may be expressed as a restriction on the average star formation rate per superbubble cross-sectional area, $\dot{\Sigma}_{\rm B} = \dot{M}_*/\pi R_{\rm B}^2$. The cooling criterion gives

$$\dot{\Sigma}_{\rm B} > \dot{\Sigma}_{\rm B,R} \simeq 0.0004 \,{\rm M}_\odot \,{\rm yr}^{-1} \,{\rm kpc}^{-2} \, n_{\rm H,0}^{7/4} R_{\rm B,100}^{3/4}$$
$$\times (\epsilon\nu_{100})^{-11/4} f_T^{15/8} (\zeta_m + 0.15)^{21/8}. \quad (37)$$

The hydrodynamical computations of Mac Low & McCray (1988) suggest for the dynamical criterion that, in terms of their dynamical variable D, the bubble velocity must exceed

the disc sound speed by a factor $D^{1/3} \simeq 4.6$, for $D > 100$. This gives

$$\dot{\Sigma}_{\rm B} > \dot{\Sigma}_{\rm B,R} \simeq 0.003 \,{\rm M}_\odot \,{\rm yr}^{-1} \,{\rm kpc}^{-2} \, T_{\rm d,4}^{3/2} \frac{n_{\rm H,0}}{\epsilon\nu_{100}}, \quad (38)$$

where $T_{\rm d,4}$ is the temperature of the ambient disc gas in units of 10^4 K. The dynamical criterion is similar to the estimate of Strickland et al. (2004a). For $n_{\rm H,0} \sim 1 - 10 \,{\rm cm}^{-3}$, these criteria give $\dot{\Sigma}_{\rm B} > 0.003 - 0.03 \,{\rm M}_\odot \,{\rm yr}^{-1} \,{\rm kpc}^{-2}$, comparable to the minimum observed star formation surface density in galaxies with winds (Veilleux et al. 2005). This raises the question: do the proxies for star formation actually probe the larger region of a superbubble, so that the minimum observed star formation surface density in galaxies with winds may be identified with the minimum $\dot{\Sigma}_{\rm B}$ required for blowout?

Differences in the hard x-ray luminosities of the wind cores are expected between the two models. In the steady-state model, the exponential sensitivity to the star formation rate results in a rapid decrease with decreasing star formation rate of the 2–10 keV luminosity when the correlation $v_\infty \simeq 700 \dot{M}_*^{1/6}$ is imposed, as shown in Fig. 6. At $E_{[2-10]{\rm keV}}/M_* \simeq 2 \times 10^{45} \text{ erg M}_\odot^{-1}$ for $\dot{M}_* = 1 \,{\rm M}_\odot \,{\rm yr}^{-1}$, the specific emissivity is up to an order of magnitude smaller than the predicted value for a superbubble with $10 < n_{\rm H,0} < 100 \,{\rm cm}^{-3}$. For $M_* = 0.1 \,{\rm M}_\odot \,{\rm yr}^{-1}$, at $E_{[2-10]{\rm keV}}/M_* \simeq 2 \times 10^{43} \text{ erg M}_\odot^{-1}$ the predicted specific emissivity in the steady state model is nearly two orders of magnitude smaller than for a superbubble with $n_{\rm H,0} \simeq 1 \,{\rm cm}^{-3}$. The hard x-ray luminosity of the wind cores may thus serve to discriminate between the models.

Both models have been scaled to a supernova ejecta mechanical energy of $10^{51}\epsilon$ erg. Observations suggest a range of $0.6 < \epsilon < 1.5$ (Arnett et al. 1989). The effects on the values of v_∞ in the steady state model or $n_{\rm H,0}$ in the superbubble model required to match observations may be inferred from the scaling relations in Eqs (7) and (24). This is a systematic uncertainty of the models, and applies as well to the predictions for radio power and metal column densities.

6.2 Radio constraints

The radio spectrum in the steady state model is expected to steepen due to the depletion of relativistic electrons by synchrotron and plasmon losses over a timescale of ~ 10 Myr. The superbubble model is computed only until the bubble emerges from the galactic disc, which is typically a much shorter time. An assessment of the long term energy losses of the relativistic electron population may be approximated by imposing energy losses over a characteristic age of 10 Myr on the bubble. Doing so shows that, because of the low gas density inside the bubble cavity, the relativistic electron population is not depleted by synchrotron or plasmon losses, so that the emission persists without steepening. Although the intrinsic electron distribution may provide a steep spectrum, this is not required. A hard spectrum near 1.4 GHz may then provide a means of discriminating between the superbubble model and the conduction-free steady state model. Such measurements are currently feasible. Probing the star-forming regions in galaxies to a distance of 20 Mpc would require an angular resolution of $1-10$ arcseconds with a sensitivity of $1-10$ mJy over a frequency range of $1-10$ GHz. These requirements are achievable with existing facilities like the Very Large Array[2] and e-MERLIN[3] for targeted observations, and are expected to become routine in survey mode with the Square Kilometre Array[4].

While both the steady state and the superbubble models are consistent with the measured radio powers for plausible values of the synchrotron model parameters, the data do not require these values. Other combinations will match the data. It is also possible other mechanisms, such as large-scale cosmic ray emission, dominate the measured power if $f_e \ll 1$. Radio measurements that resolve the star-forming regions in starbursts may help to clarify the contribution of shock-accelerated electrons within the wind-generating region to the total synchrotron radio emission.

6.3 Metal column density constraints

Imposing the approximate analytic velocity correlation $v_\infty \simeq 700\,\mathrm{km\,s^{-1}}(\epsilon^2\nu_{100}^2\dot{M}_*/R_{100})^{1/7}$ (Sec. 3.2) for the steady state model results in ion column densities depending only weakly on the star formation rate and size of the wind-generating region,

$$N_i \simeq 2.8 \times 10^{15}\,\mathrm{cm^{-2}}(\epsilon\nu_{100})^{-2/7}\nu_{100}(\dot{M}_*/R_{100})^{5/14}$$
$$\times \left(\xi_{i,\mathrm{max}}T_\mathrm{max}^{3/4}\right). \tag{39}$$

The metal column densities computed after imposing the similar numerical correlation $v_\infty = 700\,\mathrm{km\,s^{-1}}\dot{M}_*^{1/6}$ on the numerically integrated model with $R = 100$ pc are shown in Fig. 7. Commonly detected ions will have column densities between $10^{14} - 10^{16}\,\mathrm{cm^{-2}}$, comparable to those measured (Heckman et al. 2001). The ion abundances peak, however, at characteristic temperatures near the peak in the cooling curve, so that the gas will be thermally unstable. The computed column densities would then represent minimal values: as the gas condenses, the column densities will
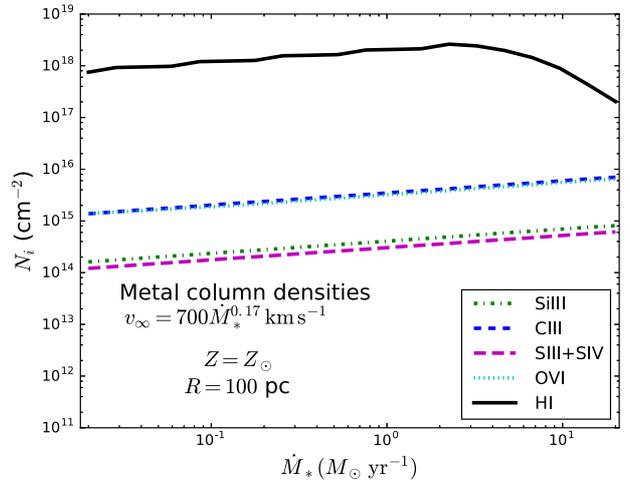

Figure 7. Column densities for selected metal ions, shown for the steady state model with $v_\infty = 700\dot{M}_*^{0.17}\,\mathrm{km\,s^{-1}}$. Also shown is the H I column density. A source region of 100 pc radius and solar metallicity are adopted.
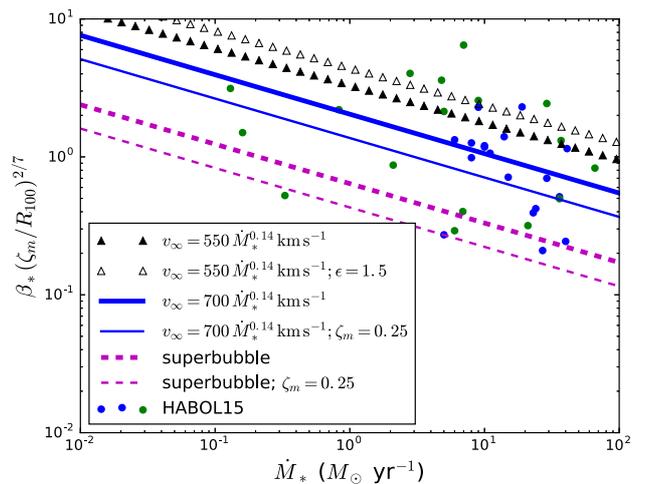

Figure 8. Mass loading factor $\beta_*(\zeta_m/R_{100})^{2/7}$ as a function of star formation rate. To allow for variations in the size $R = 100R_{100}$ pc of the star-forming regions and the gas metallicity ζ_m, the mass loading factor has been scaled by the factor $(\zeta_m/R_{100})^{2/7}$ (see text). The upper limit imposed by radiative cooling in the freely-expanding steady state model is shown for $\epsilon = 1$ (filled triangles) and $\epsilon = 1.5$ (open triangles). The predicted value in the steady state model for $v_\infty = 700\,\mathrm{km\,s^{-1}}(\epsilon^2\nu_{100}^2\dot{M}_*/R_{100})^{1/7}$ is shown for $\zeta_m = 1$ (thick blue solid line) and $\zeta_m = 0.25$ (thin blue solid line). The prediction for the superbubble model when the bubble reaches size R is shown for $\zeta_m = 1$ (thick magenta broken line) and $\zeta_m = 0.25$ (thin magental broken line). The data are from Heckman et al. (2015): the dark (blue) circles represent strong cloud outflows and light (green) circles represent weak or no cloud outflows.

[2] https://science.nrao.edu/facilities/vla
[3] http://www.e-merlin.ac.uk/
[4] http://skatelescope.org

increase, although the covering fraction of the absorption systems will decline as the gas fragments. Measurements suggest the column densities of observed systems are determined by the velocity at which they flow through coronal temperatures (Edgar & Chevalier 1986; Heckman et al. 2002), for which the column density will be of the order $(1/\sigma_i)(m_e/m_{\rm H})^{1/2}\mathcal{M}_{\rm cool}$, where $\sigma_i(T)$ is the characteristic collisional cross section of the ion, $\mathcal{M}_{\rm cool}(T)$ is the Mach number of the flow and $m_e/m_{\rm H}$ is the electron-to-proton mass ratio [5].

The neutral hydrogen column density arises from a recombination layer at $T \sim 10^4$ K that will occur at radial distances $r \simeq 76R(\epsilon\nu_{100})^{3/7}(\dot{M}_*/R_{100})^{3/14}$, typically 5–15 kpc. The layer will be optically thick to any penetrating external photoionizing radiation that may modify the predicted metal column densities, although they would still be susceptible to photoionizing radiation from the starburst. Thermal instabilities, however, may cause the layer to fragment so that its structure may become porous.

The superbubble model predicts metal column densities much smaller than measured. This was recognised by Heckman et al. (2001), who suggested dynamical instabilities as the superbubble emerges from the disc will develop turbulent mixing layers that, in sufficient number, could produce the measured column densities.

Measurements of absorption lines produced by clouds in wind outflows have been used by Heckman et al. (2015) to assess the amount of mass loading in the winds.[6] Their results are shown in Fig. 8 along with the predictions of the models. The measured values have been rescaled to account for the variation in the star-forming region sizes and the metallicities. Following the terminology of these authors, the points have also been designated as either corresponding to a strong outflow or to a weak or no outflow. The upper values lie close to the maximum allowed by cooling in the steady state model, and include many of the weak or no outflows. Adopting the correlation $v_\infty = 700\,{\rm km\,s^{-1}}(\epsilon^2\nu_{100}^2\dot{M}_*/R_{100})^{1/7}$ results in values matching the median of those measured, corresponding to strong outflows.

The lowest mass loading values lie near the value for the superbubble model, and correspond to many of the weak or no outflows. (Here, the measured star formation region is identified with the superbubble radius.) This supports the possibility that the steady-state wind is initiated by a superbubble. The high metal column densities may then arise within an outflow region at coronal temperatures, as for the steady-state wind. Further mass loading from the hydrodynamical ablation or thermal evaporation of clouds above

the plane would account for the larger mass loading factors. Observational evidence suggests thermal conduction is active within halo clouds (Marcolini et al. 2005). The clouds may have pre-existed or been accreted from larger scales, as simulations suggest entrained clouds have too short survival times to have originated in the disc (Klein et al. 1994; Scannapieco & Brüggen 2015) unless possibly supported by magnetic field pressure (Mac Low et al. 1994; McCourt et al. 2015).

7 CONCLUSIONS

Two models for the generation of galactic winds are compared. While both model the winds as powered by supernovae explosions in active areas of star formation, the models differ fundamentally in their microphysical assumptions. One neglects thermal heat conduction and treats the wind in a steady state of free expansion, as may be expected for an age large compared with the flow time. The second includes thermal heat conduction, resulting in time-dependent self-similar expansion into a surrounding medium. Observational predictions of the models are compared with x-ray, radio and UV metal line absorption measurements. The principal conclusions are summarised below.

7.1 Steady-state wind

The steady state model is characterised by two principal parameters, chosen here to be the star formation rate $\dot{M}_*$ and the asymptotic wind velocity v_∞. The wind is assumed to be generated by uniformly distributed supernovae within a core region of radius $R = 100R_{100}$ pc. The requirement that the energy generation rate exceed the cooling rate imposes a lower limit on the asymptotic velocity of $v_\infty > 550\,{\rm km\,s^{-1}}(\epsilon\nu_{100}\zeta_m\dot{M}_*R_{100}^{-1})^{0.14}$, where ζ_m is the metallicity of the wind gas relative to solar and ν_{100} and ϵ are scaling parameters describing the expected supernovae rate per star formed and their amount of energy injection. This restriction constrains the mass-loading factor to $\beta_* < 3.3(\epsilon\nu_{100})^{0.73}\zeta_m(\dot{M}_*R_{100}^{-1})^{-0.27}$.

The amount of soft x-ray energy generated per unit mass of stars formed scales approximately as $E_x/M_* \sim \dot{M}_*/(v_\infty^{1/\alpha}R)$ with $\alpha = 1/7 - 1/5$. This is contrary to the measurements of Mineo et al. (2012b), who find a constant amount of soft x-ray energy generation per unit mass of stars formed, independent of the star formation rate. The amount measured in the 0.5–2 keV band of $2 \times 10^{46}\,{\rm erg\,M_\odot^{-1}}$ is matched if the asymptotic wind velocity correlates with the star formation rate according to $v_\infty \simeq 1000\,{\rm km\,s^{-1}}(\epsilon^2\nu_{100}^2\dot{M}_*/R_{100})^\alpha$ with $\alpha \sim 1/7 - 1/5$. A lower asymptotic speed is required if the measured x-ray luminosities are reduced by extinction internal to the galaxies. Matching to the extinction-corrected 0.3–10 keV band value of $2 \times 10^{47}\,{\rm erg\,M_\odot^{-1}}$ requires $v_\infty \simeq 700\,{\rm km\,s^{-1}}(\epsilon^2\nu_{100}^2\dot{M}_*/R_{100})^\alpha$ with $\alpha \sim 1/7 - 1/5$, close to the correlation required to sustain a steady-state wind against radiative cooling and suggesting only a narrow range of mass loading is allowed for a given star formation rate. The predicted amount of hard x-ray energy generated in the

---

[5] Edgar & Chevalier (1986) and Heckman et al. (2002) argue the cooling column density is $3kTv_{\rm cool}/\Lambda(T)$, where $v_{\rm cool}$ is the flow velocity of the cooling gas and $\Lambda(T) \sim E_i\sigma_i(T)v_e(T)$ is the cooling coefficient due to electron collisional excitation of a transition with energy E_i, and v_e is the velocity of the electrons. Coronal temperatures correspond to $k_{\rm B}T \sim E_i$.

[6] The velocities of the clouds determined from the widths of their absorption features are not necessarily to be identified with the outflow velocity of the wind gas impinging on them; the clouds will generally be accelerated by ram pressure to lower velocities than the flow because of their higher densities (eg Scannapieco & Brüggen 2015).

2–10 keV band declines steeply with decreasing star formation rate, falling from $\sim 2\times10^{45}\,\mathrm{erg\,M_\odot^{-1}}$ at $\dot{M}_* = 1\,\mathrm{M_\odot\,yr^{-1}}$ to $\sim 2\times10^{43}\,\mathrm{erg\,M_\odot^{-1}}$ at $\dot{M}_* = 0.1\,\mathrm{M_\odot\,yr^{-1}}$.

The model gives a near constant amount of radio synchrotron energy at 1.4 GHz generated per unit mass of stars formed. The value is sensitive to the assumed parameters of the energy distribution function of relativistic electrons, but agreement with the data may be achieved for typical values inferred from supernova remnants. The spectrum, however, is expected to be steeper than would be given by the electron energy index for a typical wind age of 10 Myr because of the depletion of relativistic electrons within the wind-generating core by synchrotron and plasmon wave energy losses.

Except for high ionization species like O vi , commonly measured metal absorption lines such as C iii , Si iii , S iii and S iv are expected to be undetectable within the hot core of the wind. (Since the wind core resides within the galactic disc, these ions may form in detectable amounts in the disc within the interface between the wind shock front and the interstellar medium.) Detectable levels of these ions are expected from the outflow region with typical column densities of $10^{14} - 10^{16}\,\mathrm{cm^{-2}}$, weakly increasing with the star formation rate after allowing for the correlation between the asymptotic wind velocity and the star formation rate required to match the soft x-ray data. Since the gas is likely thermally and dynamically unstable in the temperature regime at which the ions form in greatest abundance, these values may set lower limits on the column densities of an increasingly fragmenting outflow.

Estimates of the amount of mass-loading from absorption line data show a maximum mass-loading factor comparable to the maximum imposed by the cooling restriction. For the approximate analytic velocity correlation $v_\infty \simeq 700\,\mathrm{km\,s^{-1}}(\epsilon^2\nu_{100}^2\dot{M}_*/R_{100})^{1/7}$, the mass loading factor is somewhat smaller than the cooling limit, $\beta_* \simeq 2.0(\epsilon\nu_{100})^{3/7}(R_{100}/\dot{M}_*)^{2/7}$, comparable to measured values and corresponding to a mass injection rate into the wind of $\dot{M} \simeq 2.0\mathrm{M_\odot\,yr^{-1}}\,(\epsilon\nu_{100})^{3/7}\dot{M}_*^{5/7}R_{100}^{2/7}$.

7.2 Superbubble with thermal heat conduction

The superbubble model may be parametrized by the star formation rate and the ambient hydrogen density into which the bubble expands within a disc galaxy. The model ceases to be directly applicable once the bubble breaks out of the disc: hydrodynamical simulations have shown instead the bubble vents its thermal energy into conical winds vertical to the disc. This will occur for expected hydrogen densities within the discs before the bubble growth is restricted by the onset of radiative cooling. The subsequent evolution of the wind is not directly computed here.

Mass loading by thermal evaporation naturally results in an amount of soft x-ray generation per solar mass of stars formed only weakly dependent on the star formation rate. Matching to the measured value in the 0.5–2 keV band requires ambient hydrogen densities of $1 - 10\,\mathrm{cm^{-3}}$, while higher densities of $10 - 100\,\mathrm{cm^{-3}}$ are required to match the measured value in the 0.3–10 keV band, after allowing for extinction corrections for internal galactic absorption. (Since extended emission out of the disc will contribute a comparable amount to the measured x-ray luminosity, the required densities may be somewhat lower.) For these densities, cooling and dynamical criteria require the star formation rate per superbubble cross-sectional area to exceed $0.003 - 0.03\,\mathrm{M_\odot\,yr^{-1}\,kpc^{-2}}$. A higher level of hard x-ray emission in the 2–10 keV band is expected for a superbubble compared with the wind core in the steady-state wind model for low star formation rates, with a value in excess of $\sim 10^{45}\,\mathrm{erg\,M_\odot^{-1}}$, and possibly as much as an order of magnitude larger or more, sustained by the superbubble for star formation rates $\dot{M}_* \sim 0.1\,\mathrm{M_\odot\,yr^{-1}}$. Such high radiative efficiencies measured in the wind cores would favour the superbubble model.

If the bubble blows out into the halo, it will do so with a thermal pressure corresponding to an effective asymptotic wind velocity, in terms of the steady-state wind parametrization, of $v_\infty^{\mathrm{eff}} \simeq 850\,\mathrm{km\,s^{-1}}(\epsilon\nu_{100}\dot{M}_*/f_T R_{\mathrm{B},100})^{1/7}$. The effective wind velocity is suggestively close to the value required for the steady state model to match the soft x-ray data. This may indicate that large-scale winds are indeed driven by superbubbles. The amount of mass loading through thermal evaporation, however, is somewhat low: $\beta_* \simeq 0.64(\epsilon\nu_{100})^{5/7}(R_{\mathrm{B},100}f_T/\dot{M}_*)^{2/7}$, corresponding to a mass injection rate of $\dot{M} \simeq 0.64\mathrm{M_\odot\,yr^{-1}}(\epsilon\nu_{100}\dot{M}_*)^{5/7}(R_{\mathrm{B},100}f_T)^{2/7}$, just somewhat smaller than the amount above for the steady state model to match the amount of x-ray energy generated per unit mass of stars formed. The value for mass loading does correspond to, and so may set, the minimal values measured from metal absorption line data. The larger measured values, however, would require additional mass loading as the wind left the disc, such as from hydrodynamical ablation or the thermal evaporation of clouds, for which there is observational evidence.

As for the steady state model, the measured 1.4 GHz radio luminosities of galaxies with winds may be recovered for plausible parameters of the relativistic electron energy distribution. Unlike for the steady state model, the relativistic electron distribution is not depleted within the wind core so that steep radio spectra are not required. This provides a possible means of distinguishing between the models.

Detectable levels of Si iii , C iii , S iii S iv and O vi in absorption are expected through the superbubble, with typical column densities of $10^{11} - 10^{14}\,\mathrm{cm^{-2}}$, nearly independent of the star formation rate and only weakly dependent on the ambient gas density and size of the superbubble. Although an ionization layer produced by a wind shock impacting on the interstellar medium of a galaxy in the steady state model may produce detectable levels of metal absorption as well, differences in the column density ratios and kinematics between the models would be expected. It is emphasized that the thermal evaporation layer in the superbubble model sets a lower limit to the metal absorption, which should have a covering fraction of order unity. The absence of the minimal predicted levels of absorption would be a telling indicator against the superbubble model. Larger values may also arise outside the disc in gas at coronal temperatures in a superbubble-driven outflow.

APPENDIX A: STEADY-STATE WIND

The equations governing a spherical wind driven by stellar winds and supernovae are:

$$\frac{\partial \rho}{\partial t} + \frac{1}{r^2}\frac{d}{dr}\left(\rho v r^2\right) = \alpha \rho_*, \tag{A1}$$

$$\rho \frac{\partial v}{\partial t} + \rho v \frac{dv}{dr} = -\frac{dP}{dr} - \rho g - \alpha \rho_* v, \tag{A2}$$

and

$$\frac{\partial}{\partial t}\left(\frac{1}{2}\rho v^2 + \rho \epsilon\right) + \frac{1}{r^2}\frac{d}{dr}\left[\rho v r^2\left(\frac{1}{2}v^2 + \frac{\gamma}{\gamma-1}\frac{P}{\rho}\right)\right] = \alpha \rho_* \langle q \rangle, \tag{A3}$$

where v, ρ, P and ϵ are the gas radial velocity, density, pressure and thermal energy per unit mass, respectively, γ is the ratio of specific heats, ρ_* is the density distribution of stars, α is the combined rate of mass loss by stars and supernovae per unit mass in stars, and $\langle q \rangle$ is the average energy injection rate by the stars and supernovae per unit mass (Burke 1968; Johnson & Axford 1971; Mathews & Baker 1971; Chevalier & Clegg 1985). For a simple wind model with the sources driving the wind confined to a region $r < R$, with $\alpha \rho_*$ and $\langle q \rangle$ constant within $r < R$ and vanishing outside, it is convenient to define the dimensionless quantities $x = r/R$, $\tilde{v} = v/\langle q \rangle^{1/2}$, $\tilde{\rho} = \rho/(\alpha \rho_* \langle q \rangle^{-1/2} V R^{-2})$ and $\tilde{P} = P/(\alpha \rho_* \langle q \rangle^{1/2} V R^{-2})$, where $V = (4\pi/3)R^3$. In terms of the energy injection efficiency ϵ and mass loading factor β of Sec. 2.1, the total energy and mass injection rates are then $\dot{E} = \epsilon \dot{E}_1 = \alpha \rho_* V \langle q \rangle$ and $\dot{M} = \beta \dot{M}_1 = \alpha \rho_* V$. Here $\dot{E}_1$ is given by an injection of $10^{51}\nu_{100}$ erg of mechanical energy per $100 M_\odot$ of stars formed along with mass injected at the rate $\dot{M}_1$. In terms of the asymptotic wind velocity v_∞, $\langle q \rangle = v_\infty^2/2$.

For a wind in a steady state with negligible gravity, the velocity and pressure at $x < 1$ may then be expressed in terms of the density as

$$\tilde{v}(x) = \frac{x}{4\pi \tilde{\rho}(x)} \tag{A4}$$

and

$$\tilde{P}(x) = \frac{\gamma-1}{\gamma}\tilde{\rho}(x)\left[1 - \frac{1}{2}\left(\frac{x}{4\pi\tilde{\rho}(x)}\right)^2\right]. \tag{A5}$$

A smooth transition from subsonic flow near the centre to supersonic flow at large x requires the Mach number $M = v/c_{\mathrm{ad}}$, where $c_{\mathrm{ad}} = (\gamma P/\rho)^{1/2}$ is the adiabatic sound speed, to satisfy $M = 1$ at $x = 1$, giving

$$\left(\frac{3\gamma+1/M^2}{1+3\gamma}\right)^{-(3\gamma+1)/(5\gamma+1)} \quad \left(\frac{\gamma-1+2/M^2}{1+\gamma}\right)^{(\gamma+1)/[2(5\gamma+1)]} \tag{A6}$$

$$= x \qquad (x < 1) \tag{A7}$$

$$M^{2/(\gamma-1)} \quad \left(\frac{\gamma-1+2/M^2}{1+\gamma}\right)^{(\gamma+1)/[2(\gamma-1)]} \tag{A8}$$

$$= x^2 \qquad (x > 1) \tag{A9}$$

(Chevalier & Clegg 1985). These equations may be solved numerically, and $\tilde{\rho}$ extracted. For $x < 1$, however, the density is well-approximated by

$$\tilde{\rho}(x) \simeq \tilde{\rho}_0 \left\{ 1 + \log\left[1 - \frac{1}{2}\frac{\gamma+1}{\gamma-1}\left(\frac{x}{4\pi\tilde{\rho}_0}\right)^2\right]^{(3\gamma+4)/(\gamma+1)} \right\}, \tag{A10}$$

where the central density $\tilde{\rho}_0 = \tilde{\rho}(0)$ is given by

$$\tilde{\rho}_0 = \frac{(3\gamma+1)^{(3\gamma+1)/(5\gamma+1)}}{4\pi(\gamma-1)^{1/2}}\left(\frac{2}{\gamma+1}\right)^{(\gamma+1)/[2(5\gamma+1)]}. \tag{A11}$$

For a monatomic gas ($\gamma = 5/3$), the central density is $\tilde{\rho}_0 = (3/2)^{1/2}(3/4)^{1/7}6^{9/14}/4\pi \simeq 0.2960$. The characteristic core radius, corresponding to $\delta(x_c) = -0.5$, is $x_c \simeq 0.98$, so that the density varies little until x approaches 1. The velocity for $x \ll x_c$ is $\tilde{v}(x) \simeq 0.2689x$ and the central pressure $\tilde{P}_0 = (2/5)\tilde{\rho}_0 \simeq 0.1184$. For $x > 1$, the solution is analytic for $\gamma = 5/3$. Defining $S_\pm(x) = [(4x)^4/2 - 64 \pm 8(4x)^2(x^4-1)^{1/2}]^{1/3}$, $U(x) = [S_+(x) + S_-(x) - 4]^{1/2}$ and $W(x) = \{2(4x)^2/U(x) - [S_+(x) + S_-(x) + 8]\}^{1/2}$, the Mach number is given by $M(x) = [U(x) + W(x)]/2$. Then

$$\tilde{v}(x) = 2^{1/2}\frac{M(x)}{[3+M^2(x)]^{1/2}}, \tag{A12}$$

$$\tilde{\rho}(x) = \frac{1}{2^{1/2}\,4\pi}\frac{[3+M^2(x)]^{1/2}}{M(x)}\frac{1}{x^2} \tag{A13}$$

and

$$\tilde{P}(x) = \frac{2^{1/2}\,3}{20\pi}\frac{1}{M(x)[3+M^2(x)]^{1/2}}\frac{1}{x^2}. \tag{A14}$$

REFERENCES

Armus L., Heckman T. M., Weaver K. A., Lehnert M. D., 1995, ApJ, 445, 666

Arnett W. D., Bahcall J. N., Kirshner R. P., Woosley S. E., 1989, Ann. Rev. Astron. Astrophy., 27, 629

Asplund M., Grevesse N., Sauval A. J., Scott P., 2009, Ann. Rev. Astron. Astrophy., 47, 481

Becker R. H., White R. L., Helfand D. J., 1995, ApJ, 450, 559

Bell E. F., 2003, ApJ, 586, 794

Brüggen M., Scannapieco E., 2016, ArXiv e-prints, 1602.01843

Burke J. A., 1968, MNRAS, 140, 241

Bustard C., Zweibel E. G., D'Onghia E., 2016, ApJ, 819, 29

Castor J., McCray R., Weaver R., 1975, ApJ, 200, L107

Chevalier R. A., 1998, ApJ, 499, 810

Chevalier R. A., Clegg A. W., 1985, Nature, 317, 44

Chevalier R. A., Fransson C., Nymark T. K., 2006, ApJ, 641, 1029

Condon J. J., 1992, Ann. Rev. Astron. Astrophy., 30, 575

Condon J. J., Cotton W. D., Broderick J. J., 2002, AJ, 124, 675

Cooper J. L., Bicknell G. V., Sutherland R. S., Bland-Hawthorn J., 2008, ApJ, 674, 157

Cowie L. L., McKee C. F., 1977, ApJ, 211, 135

Dalla Vecchia C., Schaye J., 2012, MNRAS, 426, 140

Dekel A., Silk J., 1986, ApJ, 303, 39

D'Ercole A., Brighenti F., 1999, MNRAS, 309, 941

Dopita M. A., Sutherland R. S., 1996, ApJS, 102, 161

Edgar R. J., Chevalier R. A., 1986, ApJ, 310, L27

Fabbiano G., Heckman T., Keel W. C., 1990, ApJ, 355, 442

Ferland G. J., Porter R. L., van Hoof P. A. M., Williams R. J. R., Abel N. P., Lykins M. L., Shaw G., Henney W. J., Stancil P. C., 2013, Rev. Mex. Astron. Astrof., 49, 137

Fujita A., Mac Low M.-M., Ferrara A., Meiksin A., 2004, ApJ, 613, 159

Fujita A., Martin C. L., Mac Low M.-M., Abel T., 2003, ApJ, 599, 50

Girichidis P., Naab T., Walch S., Hanasz M., Mac Low M.-M., Ostriker J. P., Gatto A., Peters T., Wünsch R., Glover S. C. O., Klessen R. S., Clark P. C., Baczynski C., 2016, ApJ, 816, L19

Grimes J. P., Heckman T., Strickland D., Ptak A., 2005, ApJ, 628, 187

Heckman T. M., Alexandroff R. M., Borthakur S., Overzier R., Leitherer C., 2015, ApJ, 809, 147

Heckman T. M., Armus L., Miley G. K., 1990, ApJS, 74, 833

Heckman T. M., Norman C. A., Strickland D. K., Sembach K. R., 2002, ApJ, 577, 691

Heckman T. M., Sembach K. R., Meurer G. R., Strickland D. K., Martin C. L., Calzetti D., Leitherer C., 2001, ApJ, 554, 1021

Howk J. C., Savage B. D., 1999, AJ, 117, 2077

Ipavich F. M., 1975, ApJ, 196, 107

Johnson H. E., Axford W. I., 1971, ApJ, 165, 381

Keller B. W., Wadsley J., Benincasa S. M., Couchman H. M. P., 2014, MNRAS, 442, 3013

Keller B. W., Wadsley J., Couchman H. M. P., 2015, MNRAS, 453, 3499

Kereš D., Vogelsberger M., Sijacki D., Springel V., Hernquist L., 2012, MNRAS, 425, 2027

Klein R. I., McKee C. F., Colella P., 1994, ApJ, 420, 213

Koo B.-C., McKee C. F., 1992, ApJ, 388, 93

Landi E., Del Zanna G., Young P. R., Dere K. P., Mason H. E., 2012, ApJ, 744, 99

Li J.-T., Wang Q. D., 2013, MNRAS, 435, 3071

Mac Low M.-M., Ferrara A., 1999, ApJ, 513, 142

Mac Low M.-M., McCray R., 1988, ApJ, 324, 776

Mac Low M.-M., McCray R., Norman M. L., 1989, ApJ, 337, 141

Mac Low M.-M., McKee C. F., Klein R. I., Stone J. M., Norman M. L., 1994, ApJ, 433, 757

Marcolini A., Strickland D. K., D'Ercole A., Heckman T. M., Hoopes C. G., 2005, MNRAS, 362, 626

Martin C. L., 1999, ApJ, 513, 156

Mathews W. G., Baker J. C., 1971, ApJ, 170, 241

McCourt M., O'Leary R. M., Madigan A.-M., Quataert E., 2015, MNRAS, 449, 2

McCray R., Kafatos M., 1987, ApJ, 317, 190

McKee C. F., Cowie L. L., 1977, ApJ, 215, 213

McKee C. F., Ostriker E. C., 2007, Ann. Rev. Astron. Astrophy., 45, 565

Meiksin A., Whalen D. J., 2013, MNRAS, 430, 2854

Meiksin A. A., 2009, Rev. Mod. Phys., 81, 1405

Miller S. T., Veilleux S., 2003, ApJS, 148, 383

Mineo S., Gilfanov M., Lehmer B. D., Morrison G. E., Sunyaev R., 2014, MNRAS, 437, 1698

Mineo S., Gilfanov M., Sunyaev R., 2012a, MNRAS, 419, 2095

Mineo S., Gilfanov M., Sunyaev R., 2012b, MNRAS, 426, 1870

Murray N., Quataert E., Thompson T. A., 2005, ApJ, 618, 569

Oppenheimer B. D., Davé R., 2008, MNRAS, 387, 577

Owen R. A., Warwick R. S., 2009, MNRAS, 394, 1741

Pittard J. M., Dyson J. E., Hartquist T. W., 2001, A&Ap, 367, 1000

Scannapieco E., Brüggen M., 2015, ApJ, 805, 158

Schiano A. V. R., 1985, ApJ, 299, 24

Shull J. M., Stevans M., Danforth C., Penton S. V., Lockman F. J., Arav N., 2011, ApJ, 739, 105

Springel V., Hernquist L., 2003, MNRAS, 339, 289

Strickland D. K., Heckman T. M., 2009, ApJ, 697, 2030

Strickland D. K., Heckman T. M., Colbert E. J. M., Hoopes C. G., Weaver K. A., 2004b, ApJS, 151, 193

Strickland D. K., Heckman T. M., Colbert E. J. M., Hoopes C. G., Weaver K. A., 2004a, ApJ, 606, 829

Strickland D. K., Stevens I. R., 2000, MNRAS, 314, 511

Suchkov A. A., Berman V. G., Heckman T. M., Balsara D. S., 1996, ApJ, 463, 528

Tomisaka K., Bregman J. N., 1993, PASJ, 45, 513

Tomisaka K., Ikeuchi S., 1988, ApJ, 330, 695

Uhlig M., Pfrommer C., Sharma M., Nath B. B., Enßlin T. A., Springel V., 2012, MNRAS, 423, 2374

Veilleux S., Cecil G., Bland-Hawthorn J., 2005, Ann. Rev. Astron. Astrophy., 43, 769

Weaver R., McCray R., Castor J., Shapiro P., Moore R., 1977, ApJ, 218, 377

Weil M. L., Eke V. R., Efstathiou G., 1998, MNRAS, 300, 773

Weiler K. W., Sramek R. A., Panagia N., van der Hulst J. M., Salvati M., 1986, ApJ, 301, 790

Zhang D., Thompson T. A., Murray N., Quataert E., 2014, ApJ, 784, 93